A fully scalable homogenization method to upscale 3-D elastic media

J Cao, R Brossier, Yann Capdeville, L Métivier, S Sambolian

Geophysical Journal International

Geophys. J. Int. (2024) **238,** 72–90
Advance Access publication 2024 April 8
GJI Seismology

https://doi.org/10.1093/gji/ggae132

A fully scalable homogenization method to upscale 3-D elastic media

J. Cao [1,*] R. Brossier,[1] Y. Capdeville [2] L. Métivier[1,3] and S. Sambolian [1,4]

[1] *ISTerre, Univsersité Grenoble Alpes, F-38000 Grenoble, France. E-mail: ludovic.metivier@univ-grenoble-alpes.fr*
[2] *CNRS, Laboratoire de Planétologie et Géosciences, Nantes Université, Université d'Angers, Le Mans Université, LPG UMR 6112, F-44000 Nantes, France*
[3] *LJK, CNRS, Univsersité Grenoble Alpes, F-38000 Grenoble, France*
[4] *CNRS, Institut Terre et Environnement de Strasbourg, Université de Strasbourg, UMR 7063, F-67084 Strasbourg, France*

Accepted 2024 April 4. Received 2024 April 2; in original form 2023 November 27

SUMMARY

Modelling seismic wavefields in complex 3-D elastic media is the key in many fields of Earth Science: seismology, seismic imaging, seismic hazard assessment and earthquake source mechanism reconstruction. This modelling operation can incur significant computational cost, and its accuracy depends on the ability to take into account the scales of the subsurface heterogeneities varying. The theory of homogenization describes how the small-scale heterogeneities interact with the seismic waves and allows to upscale elastic media consistently with the wave equation. In this study, an efficient and scalable numerical homogenization tool is developed, relying on the similarity between the equations describing the propagation of elastic waves and the homogenization process. By exploiting the optimized implementation of an elastic modelling kernel based on a spectral-element discretization and domain decomposition, a fully scalable homogenization process, working directly on the spectral-element mesh, is presented. Numerical experiments on the entire SEAM II foothill model and a 3-D version of the Marmousi II model illustrate the efficiency and flexibility of this approach. A reduction of two orders of magnitude in terms of absolute computational cost is observed on the elastic wave modelling of the entire SEAM II model at a controlled accuracy.

Key words: Finite element method; Numerical modelling; Numerical solutions; Computational seismology; Seismic anisotropy; Wave propagation.

1 INTRODUCTION

Our ability to model accurately the propagation of mechanical waves in the Earth interior is the key in many fields of seismology, such as seismic tomography and imaging (Bozdağ *et al.* 2016; Karaoğlu & Romanowicz 2018; Lei *et al.* 2020; Thrastarson *et al.* 2022; Yuan *et al.* 2014; Fichtner & Villaseñor 2015; Lu *et al.* 2020), seismic hazard risk assessment (Chaljub *et al.* 2015) and earthquake source mechanism inversion (Ide *et al.* 2011). One important question is the meaning we give to 'accurately'? In most of current applications, 'accurate' means numerically approximating the solution of 3-D elastodynamics equations in media with mechanical properties varying in the three spatial directions. The key point, specific to the Earth's interior, is the variety of the spatial scales of its mechanical properties. From microscopic grains to macroscopic tectonic units, the subsurface exhibits a continuous spectrum of heterogeneities. Simulating wavefields through such a medium by the mean of numerical approaches always relies on some types of discretization. In theory, we need to use sufficiently fine meshes to accommodate for all scales of heterogeneities, which would lead to intractable computational cost.

This is why for most applications, heterogeneities below a certain 'mesoscopic' scale are usually simply ignored. This is a rather crude approximation and a deeper understanding on how to manage this specific problem is the core of the homogenization theory, or the so-called 'equivalent media' theory. In seismology, this topic has been pioneered by Backus (1962) for the study of layered media (3-D media with spatial variations only in a single direction, usually the vertical direction in seismology). The work on non-periodic homogenization of 2-D and 3-D media was initiated in Capdeville *et al.* (2010b, 2015), respectively. What we consider in this study is an extension of this seminal work to large-scale 3-D problems. The leading idea behind homogenization is as follows: in the propagation of a band-limited wavefield, there is a threshold scale below which heterogeneities are 'seen' by the wavefields as a local smooth effective medium. In general, even for isotropic fine scales, the corresponding effective medium is fully anisotropic. The threshold scale is related to the smallest propagated wavelength. Basically, any heterogeneity smaller than half of the smallest propagated wavelength is seen as a locally smooth and anisotropic medium. It means that the wave velocity depends on the wave propagation direction locally. In the

*Now at: CGG, F-91300 Massy, France.

case of layered media studied by Backus (1962), it is possible to approximate the wave propagation by a wavefield propagating in a smoothly varying vertical transverse isotropic medium. The 3-D non-periodic homogenization theory extends this result by stating that the wave propagation in a 3-D fine-scale isotropic medium can be approximated by a wavefield propagating in an equivalent smooth anisotropic medium, where the anisotropy is generic: the equivalent medium is described by the 21 independent coefficients of the Hooke's tensor and its density (the so-called triclinic anisotropy).

This result has a deep repercussion both in the understanding of the mechanical waves we measure at the surface, and also in our capacity to model complex wave propagation phenomena in 3-D heterogeneous media. The anisotropy we observe in the seismic measurement can originate from multiple factors, from the crystalline structure of the rocks (the intrinsic anisotropy) to the specific alignment or bending of geological layers (the extrinsic anisotropy). Separating these two origins of anisotropy is difficult. It is an active research topics which goes beyond this study (Fichtner *et al.* 2013; Wang *et al.* 2013; Bodin *et al.* 2015; Alder *et al.* 2017; Magali *et al.* 2021). In any case, the band-limited data we measure should be always interpreted as propagating in an anisotropic medium, because of the presence of heterogeneities smaller than the minimum propagating wavelength. From a modelling perspective, the homogenization theory provides a tool to compute approximations of wavefields propagating in complex media with small-scale heterogeneities at a cheaper cost. This approximation can be indeed computed in a smooth anisotropic medium, for which the requirements in terms of mesh complexity are much less drastic, leading to important computational savings. This is true only if we are able to compute such equivalent media from a fine-scale isotropic represented subsurface.

How to compute this equivalent media is the main topic of the study we propose here. A series of studies (Capdeville *et al.* 2015; Cupillard & Capdeville 2018; Cupillard *et al.* 2020) have set up the theory leading to the equations for constructing the equivalent medium from a fine-scale medium. The method is derived from the two-scale homogenization theory, or formal asymptotic homogenization analysis (Sánchez-Palencia 1980) originally designed for media with a scale separation (periodic or stochastic media) and then extended to media with non-scale separation such as geological media (see Capdeville *et al.* 2020, for an introduction and a review to the method). In summary, to compute the equivalent Hooke's tensor and density, an elastostatic problem has to be solved for unitary loads on each components of the stress, leading to six elastostatic problems. From the six second-order tensors solutions of these equations, the so-called 'strain and stress concentrators' are built, which only involves algebraic operations on fourth-order tensors at each gridpoint. The last stage consists of filtering the strain and stress concentrators, the local inversion of the stress concentrators at each gridpoint, and the product of the filtered strain concentrator with the inverted filtered stress concentrators. These computations are all detailed in the next section.

From a numerical standpoint, two operations in this workflow are particularly crucial and computationally demanding: (1) the solution of the elastostatic equations, and (2) the filtering of the concentrators. These two operations are the critical part when addressing 3-D large-scale problems. In the state-of-the-art workflow proposed in Cupillard *et al.* (2020), the elastostatic problems are solved using the direct linear solver PARDISO (Schenk & Gärtner 2011). After discretization, the elastostatic equation turns into an ill-conditioned large-scale sparse linear system. A direct solver such as PARDISO is agnostic to the ill-conditioning of the matrix, making it an interesting choice. However, it suffers from the usual drawback of such numerical strategies when tackling large-scale problems: the algorithm scalability is relatively poor and the memory requirement increases in $O(N^4)$ where N is the average number of discrete points in one dimension (see, for instance, Li *et al.* 2020, for an example on frequency-domain elastic wave propagation with a direct solver). An ad hoc strategy is designed by Cupillard *et al.* (2020) to overcome this limitation when addressing large-scale problems. The domain is partitioned in smaller subdomains following a domain decomposition strategy. Each subdomain has to be sufficiently small so that the direct linear solver can be used. Each of them is considered independently with overlapping buffers to avoid boundaries artefacts. The global solution is obtained by assembling all the solutions (excluding the buffer layers) over the whole domain. Depending on the homogenization parameters, the overlapping buffers can induce a significant numerical over-cost. Regarding the filtering operation, a Gaussian smoothing through a windowed convolution is chosen for the implementation. This can be efficient on regular grids, owing to the tensorial nature of such a filter, making it possible to convert the 3-D-smoothing into a sequence of 1-D smoothing in each direction. However, on non-regular grids, such as the one which is usually considered in seismology for the solution of elastodynamics equations (namely Gauss–Lobatto–Legendre (GLL) points on hexahedral mesh used in a Spectral Element Method, SEM, Komatitsch 1997), this tensorization strategy cannot be applied anymore. Truncated convolution volumes is required, however if the correlation length is large, such truncated convolution are quickly computationally non-affordable and difficult to manage for efficient parallel implementation with domain decomposition.

An alternative to the finite-element type solution above is the fast Fourier homogenization method (Capdeville *et al.* 2015). The method is derived from Moulinec & Suquet (1998). The solution of the elastostatic part is based on a Lippmann–Schwinger equation which can be solved efficiently in the wavenumber domain, through fast Fourier transform, with a computational cost scaling in $O((N\log(N))^3)$. The Lippmann–Schwinger decomposition is solved iteratively, though, with a convergence which depends on the media roughness (contrasts in mechanical properties). The filtering part is trivial and performed directly in the wavenumber domain. This method is very efficient as long as the computation fits within a shared memory computer. For larger domain, the same domain decomposition strategy as for the finite-element type solver needs to be employed, with the same buffer layers issue.

In this study, we propose to overcome these limitations by the use of systematically scalable numerical strategies, relying on a domain decomposition algorithm. The core of the method relies on the analogy of different partial differential equations systems. The common denominator is the system of elastodynamics equations. The elastostatic equations which need to be solved correspond to a static version of these equations where the mass-acceleration term is set to zero. The filtering operation we use is based on the Bessel filter proposed by Trinh *et al.* (2017). Again, behind this filter, the Bessel equation can be seen as a static equation similar to the elastostatic equation. In addition, we discuss how to obtain a low-pass filter which approximates the response of a Gaussian filter in the wavenumber domain by composing and scaling different Bessel's filter. We perform a specific numerical analysis of this problem and solve it using a global optimization algorithm.

In the context of the SEISCOPE project, we have developed the full waveform modelling and inversion package 'SEM46' for elastodynamics equation (Trinh *et al.* 2019; Cao *et al.* 2022b). It is based on a spectral-element discretization and a domain decomposition

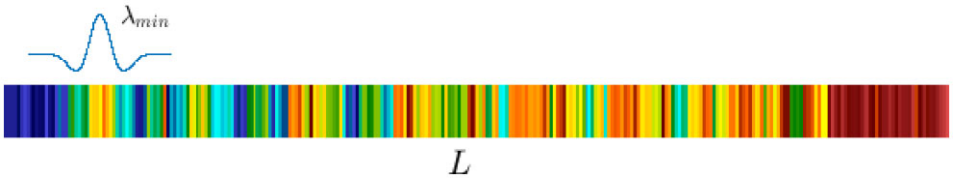

Figure 1. Schematic illustration of 1-D non-periodic homogenization. Series of heterogeneous fine layers in a finite 1-D medium of length L in which a zeroth-order homogenized solution of a wavefield with minimum wavelength $\lambda_{\min} < L$ could be analytically derived.

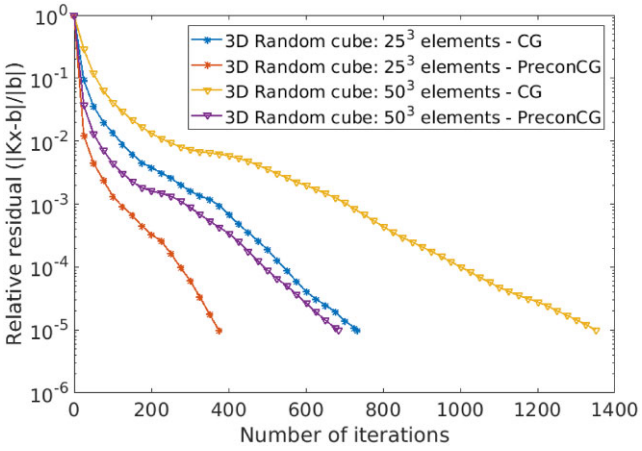

Figure 2. Convergence comparison of the conjugate gradient method with and without the diagonal pre-conditioner (PreconCG and CG) for the solution of the elastostatic equations. The 3-D random model described in Section 4.1 is used here, with two mesh sizes: one with 25^3 elements, and the other with 50^3 elements.

strategy ensuring an excellent scalability. The most computationally intensive part of the full waveform modelling solver is related to the stiffness matrix-vector product which needs to be performed at each time-marching iteration. This matrix-vector product has been carefully optimized, based on loop unrolling (Deville *et al.* 2002), cache optimization (Tarayoun *et al.* 2022) and parallelism thanks to domain decomposition. Owing to the above-mentioned analogy between the mathematical structure of the operators involved in the homogenization process, we can re-exploit the computational kernel optimized for the elastodynamic equations to obtain a fully scalable homogenization process. To re-exploit it, we simply need to rely on an iterative solver for the solution of the resulting linear systems after discretization of the elastostatic and Bessel equations. Thanks to the symmetric positive definiteness (achieved by choosing appropriate boundary conditions in the elastostatic case), a matrix-free conjugate gradient solver is implemented.

Another advantage of the technique we propose is that all the operations are performed directly on the spectral-element mesh, without need to project back and forth on a Cartesian grid. The latter operation can be time-consuming and inaccurate. Working directly on the spectral-element mesh, the homogenization routine can be directly integrated in the full waveform modelling and inversion package SEM46, which makes it very easy to use.

To illustrate the efficiency of our approach, we first present a validation test on a 3-D random media, which is a homogeneous medium with randomly located cubic fine-scale perturbations, with random amplitude. We perform a convergence test in terms of homogenization theory (convergence of the solution in the equivalent medium towards the solution in the fine-scale model), and a scalability test. Both illustrate the good behaviour of the proposed method. Second, we illustrate the effectiveness of the strategy by considering the homogenization of the entire SEAM II foothill model. Thanks to the scalability and the flexibility of our implementation, we manage to homogenize an unprecedented large-scale model containing almost 15 billions of unknowns. We compare the computation cost for a 4 Hz central frequency signal in the fine-scale model and the smooth equivalent model, and find a gain approximately equal to 300 times in terms of computational hours per core considering the modelling time only and not the time spent to build the homogenized model. Finally, we also consider the case of a fluid/solid coupling modelling in a 3-D version of the Marmousi II model. Although the homogenization theory is designed for elastic media only, we present a strategy to use it in this marine context, where a layer of fluid is located above the elastic medium. We explicitly apply homogenization to the elastic part only, and find that the resulting simulation in the homogenized medium converges towards the simulation in the fine-scale model. Given the ongoing interest for ocean-bottom-station data in exploration scenario and imaging of the deep crust, this result should have an important impact in both communities.

In Section 2, we start by a short review of the non-periodic homogenization theory in the 1-D and 3-D cases, respectively. Then in Section 3, we present the methodology we propose to solve for the 3-D homogenization problem. We first explicit the analogy between elastodynamics, elastostatic and Bessel equations, which is the core of our strategy. We then present in details how we solve the elastostatic equation with a conjugate gradient iterative solver, and how we design a low-pass filter to approximate a Gaussian filter by the composition of several Bessel filters. In Section 4, we show how our method can be used to solve for large-scale 3-D homogenization problems. After performing a convergence analysis, we investigate the homogenization of the entire SEAM II Foothill model, involving several billions of discrete parameters, before we consider the homogenization for fluid/solid problem based on a 3-D extension of the Marmousi II model.

2 REVIEW OF THE NON-PERIODIC HOMOGENIZATION THEORY

2.1 The 1-D case

The field of non-periodic homogenization dates back to the computation of effective properties for composite materials in micromechanics (Bensoussan *et al.* 1978). Its application to the modelling of the propagation of mechanical waves in solids is derived later by Capdeville *et al.* (2010a, b) and Cupillard & Capdeville (2018) with the objective to upscale any 1-D, 2-D and 3-D elastic media without size, shape and contrast restrictions on the heterogeneities. We start this study by a brief overview of this non-periodic homogenization theory in mechanics in the 1-D case. This makes it possible to recall the main concepts in the non-periodic homogenization.

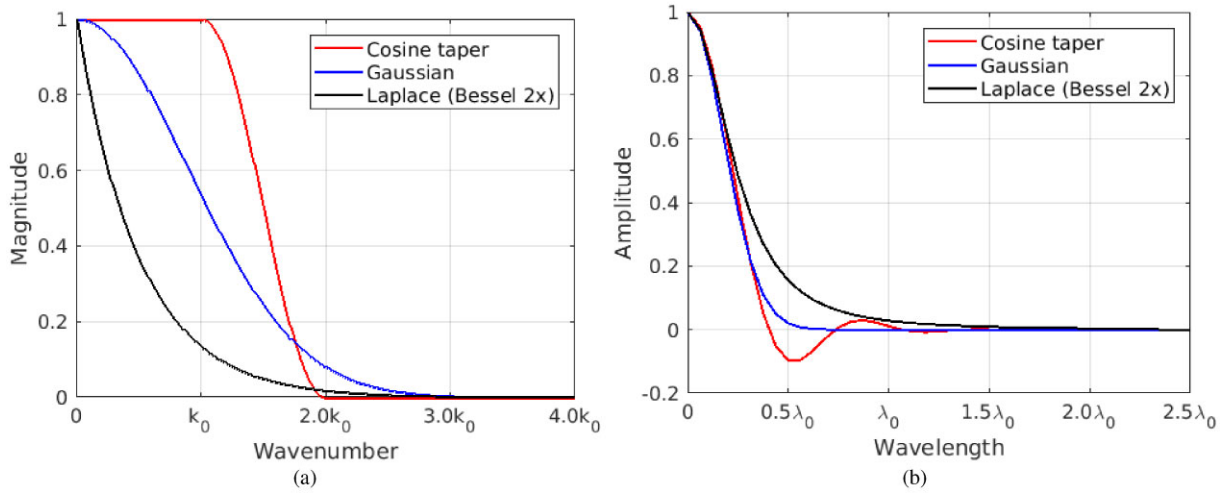

Figure 3. (a) Wavenumber spectra $\hat{w}^{\lambda_0}$ and (b) corresponding wavelets w^{λ_0} for three low-pass filters: Cosine-tapered filter, Gaussian filter and Laplace filter implemented by a cascade of two Bessel filters, with $2.5\lambda_0$ spatial support.

Table 1. The pre-conditioned parallel CG method for computing the six correctors χ^{pq}. The computer intensive part is the computation of $\mathbf{y}$ by matrix-vector product involving the matrix $\mathbf{K}$. This operation is separated from the others in lines 10 and 16 to identify it clearly. We see that the number of such matrix-vector product is equal to $k+1$ after k iterations for each corrector χ^{pq}. All the other operations are vector based: scalar products between vectors, addition of two vectors, multiplication by a constant and multiplication by a diagonal matrix.

1:	**for** p = 1 to 3 **do**
2:	**for** q = p to 3 **do**
3:	Initialize $\boldsymbol{\chi}^{pq} = \mathbf{0}$, load medium parameter $\mathbf{m} = (\mathbf{C}, \rho)$
4:	Build right-hand side vectors $\mathbf{F}^{pq}(\mathbf{m})$
5:	**end for**
6:	**end for**
7:	Build the preconditioner $\mathbf{P} = (\text{diag}(\mathbf{K}))^{-1}$
8:	**for** p = 1 to 3 **do**
9:	**for** q = p to 3 **do**
10:	$\mathbf{y} = \mathbf{K}\boldsymbol{\chi}^{pq}$
11:	$\mathbf{r}^{pq,0} = \mathbf{b}^{pq} - \mathbf{y}$
12:	$\mathbf{z}^{pq,0} = \mathbf{P}\mathbf{r}^{pq,0}$
13:	$\mathbf{p}^{pq,0} = \mathbf{z}^{pq,0}$
14:	$k = 0$
15:	**do while** ($\sqrt{\|\mathbf{r}^{pq,k}\|^2/\|\mathbf{b}^{pq,k}\|^2} > tol$ .AND. $k <$iter_max)
16:	$\mathbf{y} = \mathbf{K}\mathbf{p}^{pq,k}$
17:	$\alpha = \frac{(\mathbf{r}^{pq,k})^T \mathbf{z}^{pq,k}}{(\mathbf{p}^{pq,k})^T \mathbf{y}}$
18:	$\boldsymbol{\chi}^{pq,k+1} = \boldsymbol{\chi}_i^k + \alpha \mathbf{p}_i^k$
19:	$\mathbf{r}^{pq,k+1} = \mathbf{r}^{pq,k} - \alpha \mathbf{y}$
20:	$\mathbf{z}^{pq,k+1} = \mathbf{P}\mathbf{r}^{pq,k+1}$
21:	$\beta = \frac{(\mathbf{r}^{pq,k+1})^T \mathbf{z}^{pq,k+1}}{(\mathbf{r}^{pq,k})^T \mathbf{z}^{pq,k}}$
22:	$\mathbf{p}^{pq,k+1} = \mathbf{z}^{pq,k} + \beta \mathbf{p}^{pq,k}$
23:	$k = k + 1$
24:	**end do**
25:	**end for**
26:	**end for**

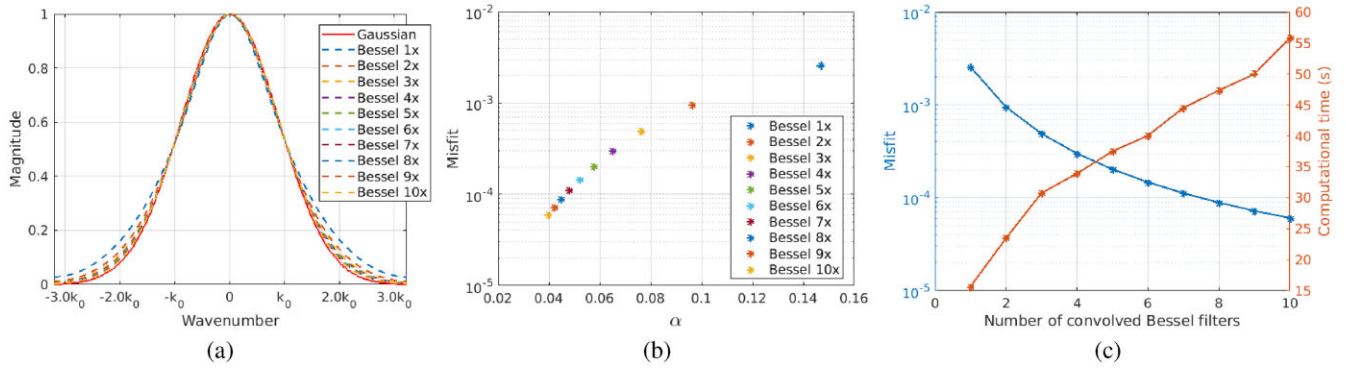

Figure 4. (a) Approximation of the Gaussian filter through a cascade of Bessel filters and their corresponding misfits with respect to the stretching factor α and number of Bessel filters N (b) which are calculated by solving a wavenumber response fitting problem. As a compromise in terms of the approximation accuracy (blue) and computational cost (orange), we superpose these two curves in (c), and their intersection is between Bessel 4x with $\alpha = 6.496 \times 10^{-2}$ and Bessel 5x with $\alpha = 5.752 \times 10^{-2}$.

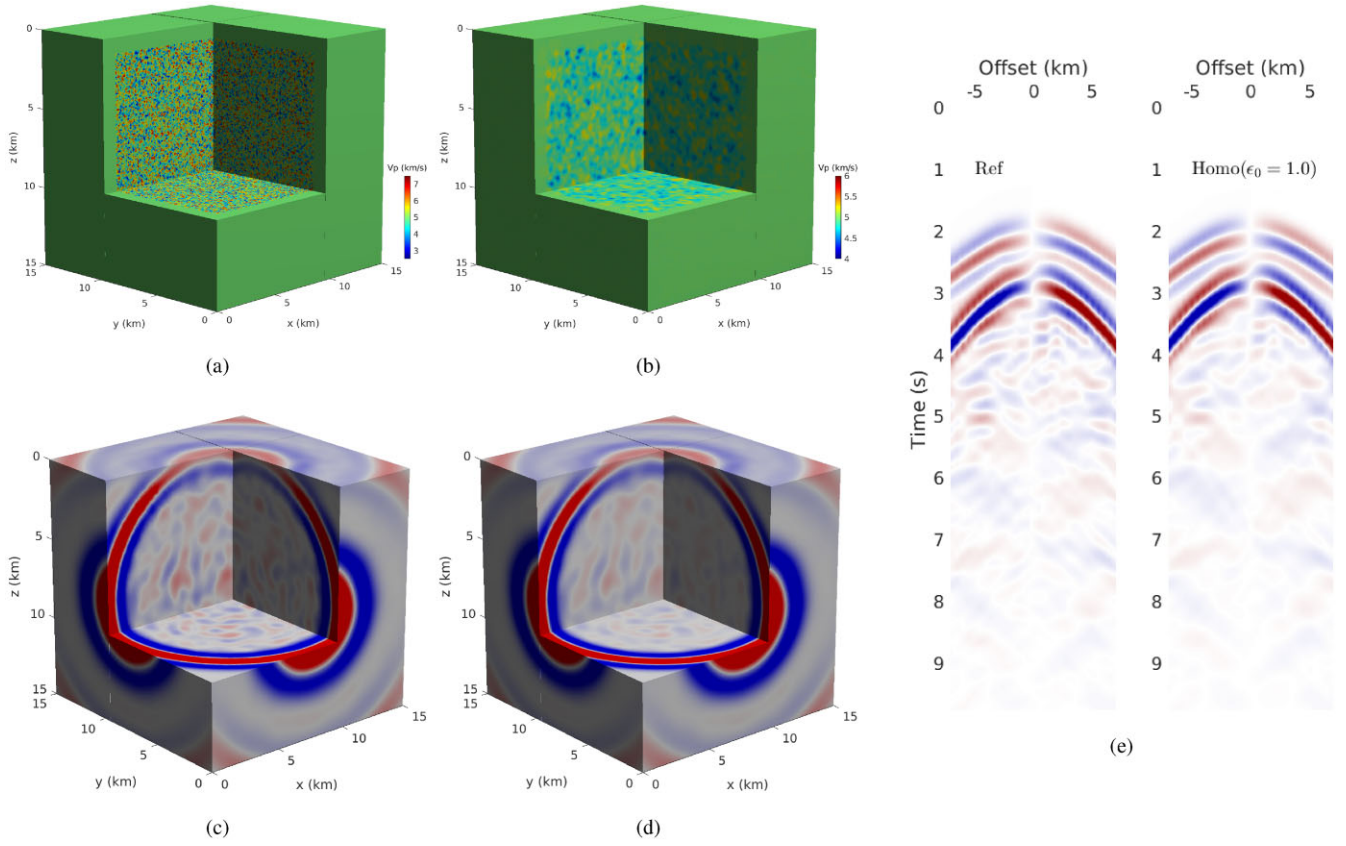

Figure 5. Homogenization in the 3-D isotropic random model. (a) The original P-wave velocity model V_p and (b) its effective 'vertical' V_p model ($V_p = \sqrt{\frac{c^{*,\varepsilon_0}_{3333}}{\rho}}$) obtained by the proposed homogenization process with $\varepsilon_0 = 1.0$, corresponding to $\lambda_0 = \varepsilon_0 \lambda_{\min}$. (c) and (d) illustrate snapshots of the vertical displacement wavefield generated from the original random model and effective model with $\varepsilon_0 = 1.0$, respectively, and (e) is a comparison of their horizontal displacement wavefields in terms of shot gather (receiver line placed along the x-direction with 1 km depth).

Let us consider the wave propagation in a finite 1-D bar of length L, composed of N heterogeneous fine layers (Fig. 1). The 1-D wave equation in such an elastic medium is given by

$$\begin{aligned} \rho \partial_{tt} u - \partial_x \sigma &= b, \\ \sigma &= E \partial_x u, \end{aligned} \tag{1}$$

where the medium parameters are Young's modulus $E(x)$ and density $\rho(x)$, $\sigma(x, t)$ is the traction field, $u(x, t)$ is the particle displacement field, and $b(x, t)$ is the source term. We consider a point source (localization in space) at x_S with a time signature given by a Ricker wavelet such that

$$b(x, t) = \delta(x - x_S) r(t), \tag{2}$$

with the Ricker wavelet $r(t) = \left(1 - 2\pi^2 f_0^2 (t - t_0)^2\right) e^{-\pi^2 f_0^2 (t - t_0)^2}$. The function $\delta(x)$ is the Dirac delta function, f_0 is the central frequency of the Ricker, and t_0 is a time-shift to make the Ricker function causal ($r(0) \simeq 0$). The frequency content of the Ricker wavelet has a compact support in the frequency domain, and it is

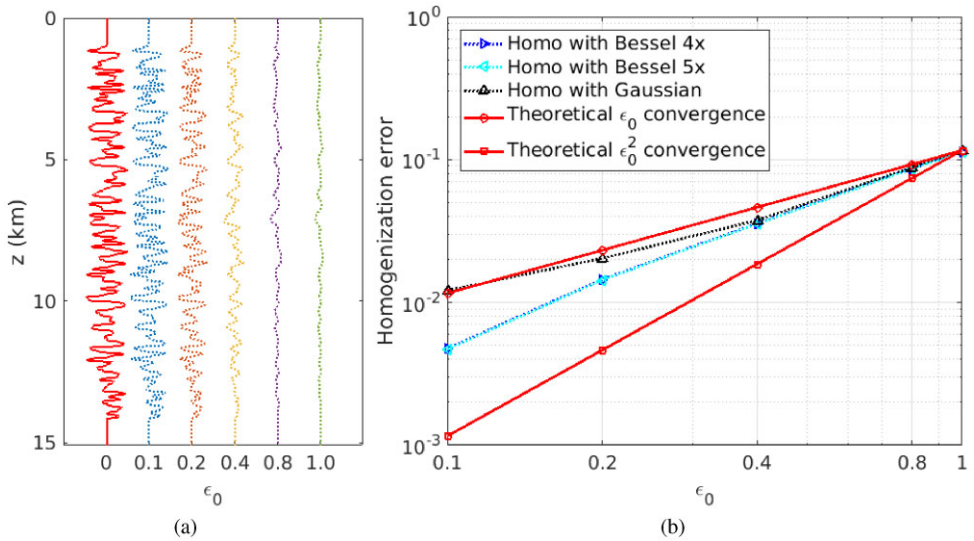

Figure 6. Convergence test of the homogenized solution with respect to ε_0. (a) 1-D depth profile illustration of effective 'vertical' *P*-wave velocity models V_p^* taken in the centre of the cube, where $\varepsilon_0 = 0$ corresponds to the original isotropic *P*-wave velocity V_p. (b) Relative error between wavefields computed in the homogenized model and the reference wavefield computed in the fine-scale isotropic model using three types of low-pass filter strategies: the Gaussian filter, and its approximation through 4 and 5 Bessel's filter applied in cascade.

Table 2. Discretization and computational cost of the CG-based iterative homogenization process in the 3-D random model validation test. Although we run the test with different ε_0 from 0.1 to 1.0 for a quantitative convergence study, the changing of ε_0 only influences the number of CG iteration for low-pass filtering the concentrators (more number of iterations for a higher ε_0), which is around 10 per cent cost of the total process. The elapsed time which is given is the average over the homogenization for different ε_0. These tests have been performed on the SWAN platform of Cray Marketing Partner Network with Intel Cascade Lake CPU architecture (2.5G Hz, 40 CPU cores per node).

Mesh (elements)	Element size	Solution space (DOF)	CG iterations for solving elastostatic equations						CG iterations for low-pass filtering	Average elapsed time (s)
			$\mathbf{b}^1$	$\mathbf{b}^2$	$\mathbf{b}^3$	$\mathbf{b}^4$	$\mathbf{b}^5$	$\mathbf{b}^6$		
$161 \times 161 \times 161$	100 m (the scale of random cubes)	810 million	1514	1500	1531	1508	1510	1509	$\leq$800	1099

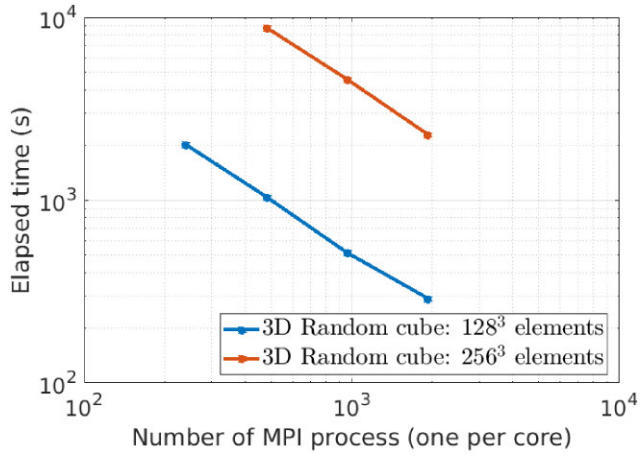

Figure 7. Strong scalability tests for the homogenization process on the 3-D random model validation test. We measure the elapsed time with respect to the number of CPU cores used, with two different meshes: one with 128^3 elements, and the second with 256^3 elements. In both cases, the scalability is close to be linear. The tests are run on SWAN platform of Cray Marketing Partner Network with Intel Cascade Lake CPU architecture (2.5G Hz, with 40 CPU cores per node).

usual to consider that the maximum frequency at which the energy is non-zero is given by

$$f_{\max} = 2.5 f_0. \tag{3}$$

From this maximal frequency, the signal propagated in the 1-D bar is bandlimited, and there exists a minimum wavelength $\lambda_{\min}$ such that

$$\lambda_{\min} = \frac{c_{\min}}{f_{\max}}, \tag{4}$$

with $c_{\min}$ the minimum velocity in the bar, related to the Young's modulus $E(x)$ and the density $\rho(x)$ by

$$c_{\min} = \min_x \sqrt{\frac{E(x)}{\rho(x)}}. \tag{5}$$

Linear elasticity theory imposes specific conditions at all medium discontinuities (*i.e.* between each layers). These conditions are the continuity of the displacement and traction fields. We denote by x_i, $i = 1, \ldots, N-1$ the position of each interface between the layer i and the layer $i+1$. These conditions can be expressed by

$$[u](x_i, t) = 0, \qquad [\sigma](x_i, t) = 0, \quad i = 0, \ldots, N, \tag{6}$$

Table 3. Strong scalability tests for the homogenization process on the 3-D random model validation test. Detailed statistic from Fig. 7. We measure the elapsed time with respect to the number of CPU cores used, with two different meshes: one with 128^3 elements, and the second with 256^3 elements. In both cases, the scalability is close to be linear. The tests are run on SWAN platform of Cray Marketing Partner Network with Intel Cascade Lake CPU architecture (2.5G Hz, with 40 CPU cores per node).

Mesh (elements)	Element size	Solution space (number of DOF)	Elapsed time (s) 240 CPU cores	480 CPU cores	960 CPU cores	1920 CPU cores
$128 \times 128 \times 128$	100 m	410 million	2013	1042	516	290
$256 \times 256 \times 256$	50 m	3.24 billion	N/A	8800	4588	2293

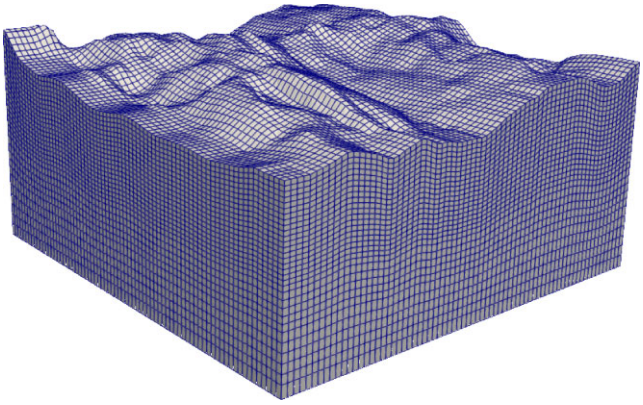

Figure 8. Schematic of the deformed Cartesian-based structured mesh to conform the strong topography variation.

where for a given field $v(x, t)$, $[v](x, t)$ denotes the 'jump' across x at time t

$$[v](x,t) = v(x^+,t) - v(x^-,t). \tag{7}$$

We also impose periodic boundary conditions at $x = 0$ and L (Capdeville *et al.* 2010a). In the above settings, the non-periodic homogenization theory provides the following zeroth-order effective wave equation

$$\begin{aligned} \rho^* \partial_{tt} u^0 - \partial_x \sigma^0 &= b^*, \\ \sigma^0 &= E^* \partial_x u^0, \end{aligned} \tag{8}$$

where ρ^* and E^* are the so-called zeroth-order long-wavelength equivalent effective density and Young's modulus and b^* the effective source term. A step-by-step tutorial describing how to obtain this result is provided in Capdeville *et al.* (2020).

In the following, we use $b^* = b$, but in general, to be consistent, the source term needs to be a modified point source (Capdeville *et al.* 2010a, b; Burgos *et al.* 2016) or an effective distributed source (Capdeville 2021). This is a zeroth-order approximation in the sense that it can be proved that the solution $u(x, t)$ of the fine-scale problem and the solution $u^0(x, t)$ of the effective wave equation are related by

$$u(x,t) = u^0(x,t) + \varepsilon_0 \mathcal{R}\left(x, \frac{x}{\varepsilon_0}, t\right), \tag{9}$$

with $\mathcal{R}(x, t)$ a residual function. In eq. (9), ε_0 controls the accuracy of the approximation u^0. It is the key parameter to compute the long-wavelength equivalent effective density $\rho^*(x)$ and Young's modulus $E^*(x)$ as

$$\rho^* = \mathscr{F}^{\varepsilon_0}(\rho), \qquad E^* = \left[\mathscr{F}^{\varepsilon_0}\left(\tfrac{1}{E}\right)\right]^{-1}, \tag{10}$$

where $\mathscr{F}^{\varepsilon_0}$ is a filter which removes any heterogeneities of a scale below λ_0 such that

$$\lambda_0 = \varepsilon_0 \lambda_{\min}. \tag{11}$$

The formulae for the effective density and Young's modulus, and the parameter ε_0 are introduced in Capdeville *et al.* (2010a). The latter controls the accuracy of the homogenization approximation. The smaller ε_0 is, the better the approximation u^0 is. In turns, the effective medium parameters $\rho^*(x)$ and $E^*(x)$ contain smaller heterogeneities. On the opposite, when ε_0 is large, the effective medium parameters $\rho^*(x)$ and $E^*(x)$ are smoother, but the approximation u^0 might be less accurate. This trade-off between accuracy and smoothness of the effective medium parameters is inherent to the non-periodic homogenization. One shall keep in mind that the forsaken reduction in computational cost comes from the smoothness of the effective medium parameters which makes it possible to use much coarser meshes as the one which would be required to model the propagation of waves in the fine-scale medium. Usually, a choice of $\varepsilon_0 = 0.5$ gives a good trade-off: any heterogeneities below half the minimum wavelength are removed from the effective medium parameters, yielding a good approximation and a simplification of the medium properties. What is interesting to see already is also that the effective density is simply a low-passed filtered version of the fine-scale density, while the effective stiffness (Young's modulus) requires a more complicated operation (inverse of the smoothed inverse).

2.2 3-D generalization

The generalization of this concept to 2-D and 3-D is investigated in Capdeville *et al.* (2010b, 2015), Capdeville (2016) and Cupillard & Capdeville (2018) with an example on the SEG/EAGE overthrust model presented in Cupillard *et al.* (2020). The propagation of mechanical waves in a 3-D elastic media are described by the following elastodynamics equations

$$\begin{aligned} &\rho \partial_{tt} u_i - \sum_{j=1}^{3} \partial_j \sigma_{ij} = b_i, \quad i = 1, \ldots 3, \\ &\sigma_{ij} = \frac{1}{2} \sum_{k=1}^{3} \sum_{l=1}^{3} c_{ijkl} \left(\partial_k u_l + \partial_l u_k\right), \quad i = 1, \ldots, 3, \quad j = 1, \ldots, 3, \end{aligned} \tag{12}$$

or, equivalently, eliminating the stress

$$\rho \partial_{tt} u_i - \frac{1}{2} \sum_{j=1}^{3} \partial_j \sum_{k=1}^{3} \sum_{l=1}^{3} c_{ijkl} \left(\partial_k u_l + \partial_l u_k\right) = b_i, \quad i = 1, \ldots 3. \tag{13}$$

The mechanical properties now correspond to the density $\rho(\mathbf{x})$, where $\mathbf{x} \in \mathbb{R}^3$, and the fourth-order Hooke's tensor $c_{ijkl}(\mathbf{x})$. The displacement wavefield $u(\mathbf{x}, t)$ has three components, and the stress

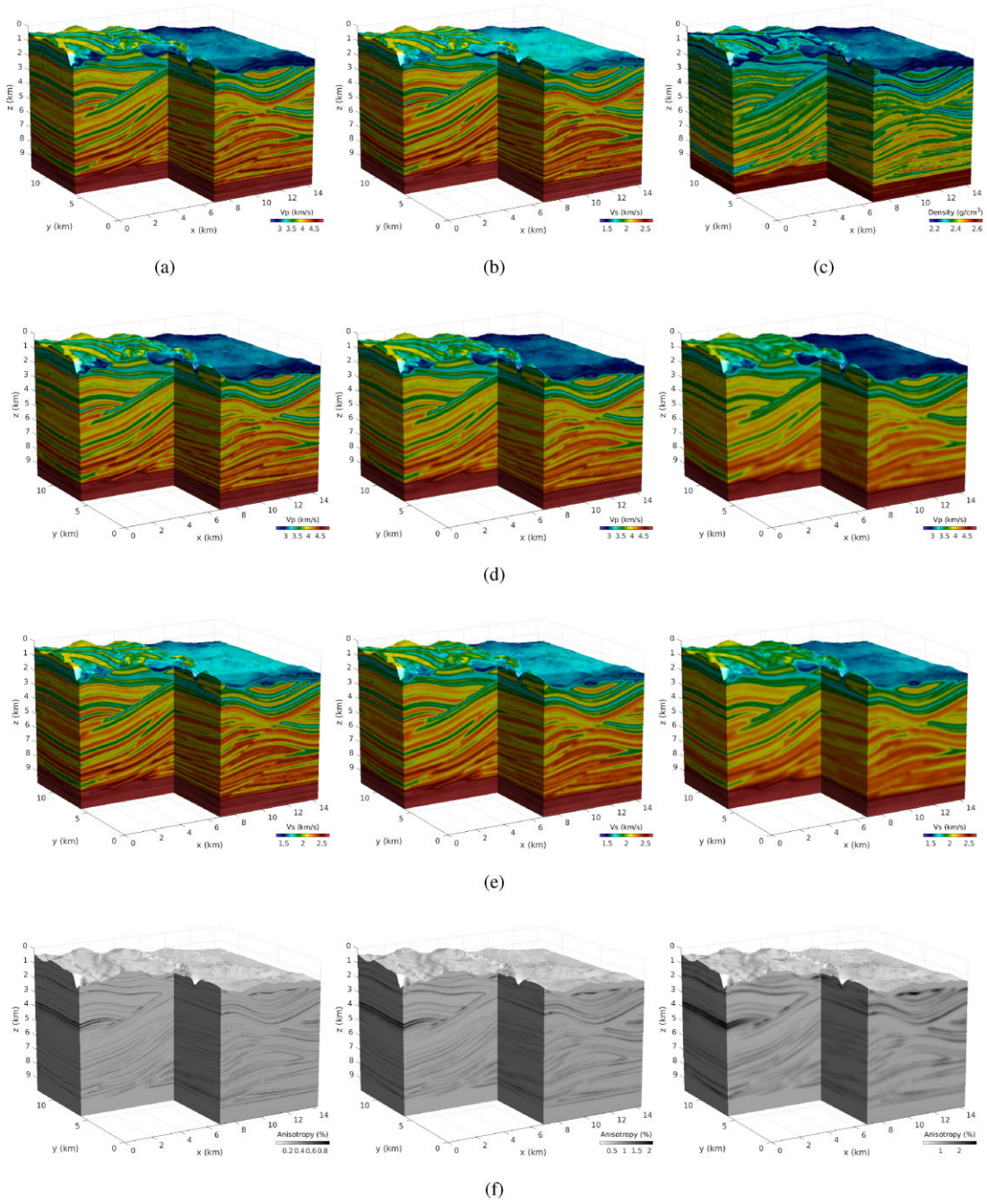

Figure 9. 3-D SEAM-II onshore models and its effective models after the homogenization process. (a)–(c) are the original *P*-wave velocity V_p, *S*-wave velocity V_s and density models. (d)–(f) are effective models of V_p, V_s and the total anisotropy in percentage obtained with $\varepsilon_0 = 0.25$, 0.5 and 1.0 from left to right, respectively. They are calculated by projecting the resulting elasticity tensor coefficients $\boldsymbol{c}^{*,\varepsilon_0}$ from the homogenization process to the closest isotropic model (Browaeys & Chevrot 2004). The effective models of density are not shown, since they are obtained by simply low-pass filtering the original density according to the homogenization theory.

tensor $\sigma(\mathbf{x}, t)$ is a symmetric three-by-three matrix, hence containing six independent coefficients $\sigma_{ij}(\mathbf{x}, t)$.

Reviewing the mathematical derivation of the long-wavelength equivalent coefficients $\rho^*(\mathbf{x})$ and $c^*_{ijkl}(\mathbf{x})$ through the homogenization theory is beyond the scope of this study and is now well established. Here, we only summarize the numerical procedure to compute these coefficients, with the objective to make each step explicit, avoiding general high-order tensorial notations which tend sometimes to obscure the nature of the operations involved. For this reason, we make the decision in this study not to rely on the Einstein summation convention and to make each summation explicit.

The homogenization procedure for 3-D media can be decomposed in the following three steps:

(i) Step 1: solve the elastostatic equations (so-called cell problems) with periodic boundary conditions for the so-called first-order corrector tensor χ^{pq}, $p, q = 1, \ldots, 3$. The corrector's components

Table 4. Discretization and computational cost for the CG-based iterative homogenization process on the challenging 3-D SEAM II model with $\varepsilon_0 = 0.5$. The test is run on Jean Zay (HPE SGI 8600 supercomputer from IDRIS, CNRS) using 7680 CPU cores with Intel Cascade Lake CPU architecture (2.5G Hz, 40 CPU cores per node).

Mesh (elements)	Element size	Solution space (DOF)	CG iterations for solving elastostatic equations						CG iterations for low-pass filtering	Elapsed time (s)
			$\mathbf{b}^1$	$\mathbf{b}^2$	$\mathbf{b}^3$	$\mathbf{b}^4$	$\mathbf{b}^5$	$\mathbf{b}^6$		
349 × 502 × 436	30 m (the smallest heterogeneity scale)	14.69 billion	12613	12482	11983	12998	13623	12720	≤420	10 668

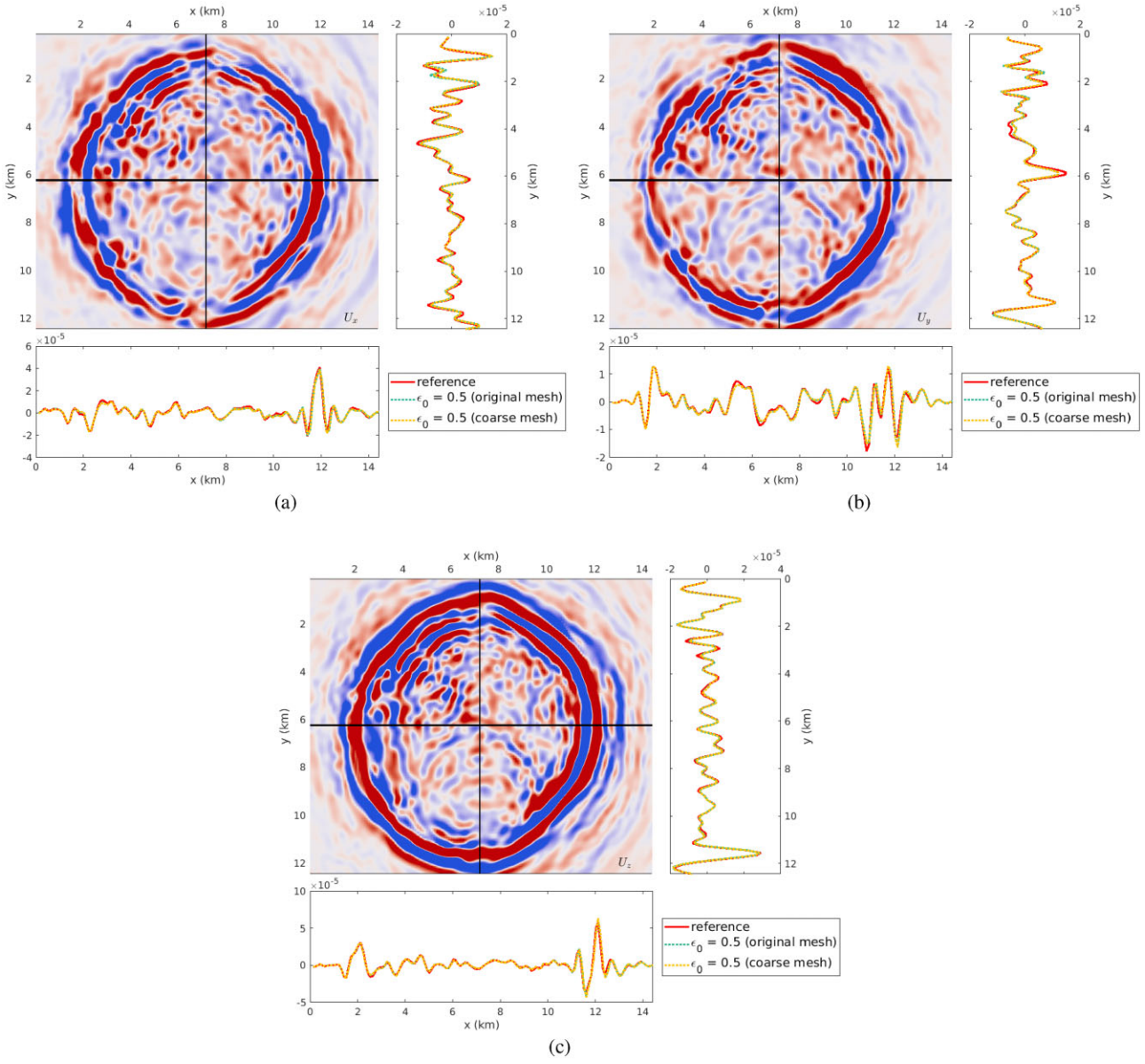

Figure 10. Snapshots of the 3C displacement wavefields u_x (a), u_y (b) and u_z (c) at the surface topography generated from the original SEAM-II model with a mesh of 339 × 502 × 436 elements and its effective models by using $\varepsilon_0 = 0.5$ in the homogenization process with two different mesh configurations in the modelling (the same mesh of 339 × 502 × 436 elements as for the original model and a coarse mesh of 66 × 119 × 106 elements adaptive to the local velocity of the homogenized V_s model).

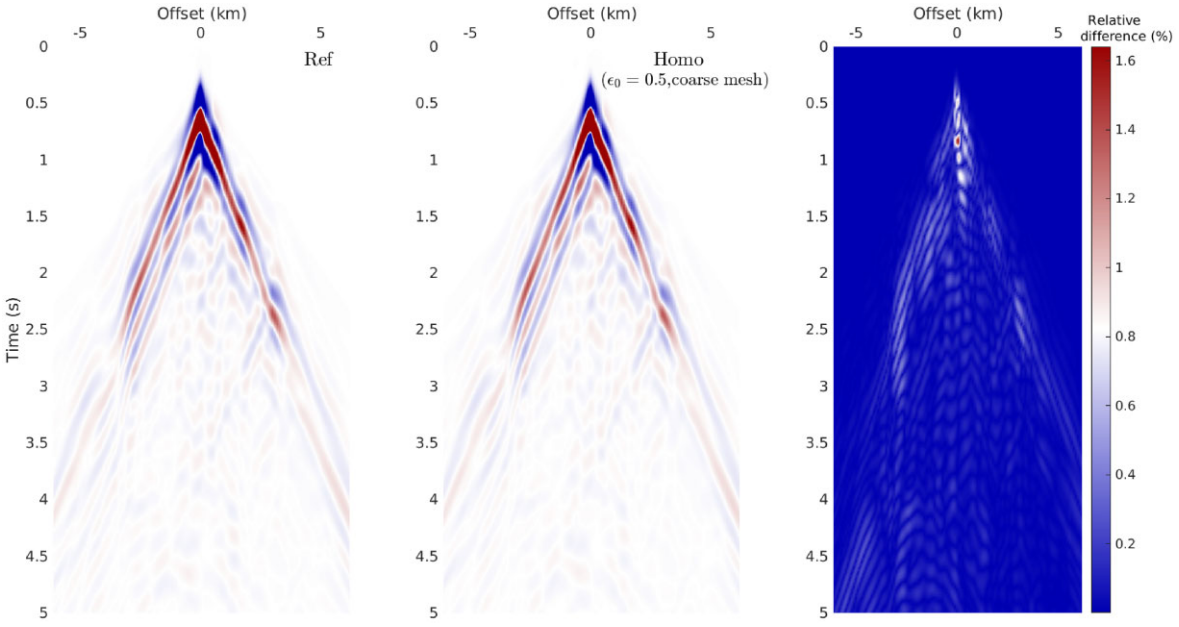

Figure 11. Shot gather comparison of the vertical displacement wavefields u_z recorded at the surface topography with $x = 7.33$ km. Left-hand panel: the gather generated from the original SEAM-II model with a mesh of $339 \times 502 \times 436$ elements. Middle panel: the gather generated from its equivalent model by using $\varepsilon_0 = 0.5$ in the homogenization process on a coarse mesh of $66 \times 119 \times 106$ elements adaptive to the local velocity of the homogenized V_s model). Right-hand panel: the relative difference between 'Ref' and 'Homo' presented in percentage.

Table 5. Computational cost for modelling in the fine mesh and the coarse mesh for the SEAM II model. Total CPU hours are calculated by the product of elapsed time and total number of CPU cores. It quantifies the computational complexity and can be interpreted as the elapsed time when using a single CPU core only. Both tests are run on Jean Zay (HPE SGI 8600 supercomputer from IDRIS, CNRS) with Intel Cascade Lake CPU architecture (2.5G Hz, 40 CPU cores per node).

Model	Mesh ($x \times y \times z$)	Element size (m)	dt (ms)	NT	Cores	Elapsed time (min)	Total CPU hours
Fine scale	$339 \times 502 \times 436$	30	0.25	20 000	2,560	97.99	4181
Homogenized	$66 \times 119 \times 106$	127.98–254.73	1.25	4000	160	5.22	13.9

χ^{pq} are homogeneous to displacement fields, with three components.

$$\begin{aligned} &\frac{1}{2}\sum_{j=1}^{3}\partial_j \sum_{k=1}^{3}\sum_{l=1}^{3} c_{ijkl}\left(\partial_k \chi_l^{pq} + \partial_l \chi_k^{pq}\right) = F_i^{pq}, \quad i = 1, \ldots 3, \\ &F_i^{pq} = \sum_{j=1}^{3} \partial_j c_{ijpq}, \quad i = 1, \ldots 3. \end{aligned} \tag{14}$$

Because of the minor symmetry of the Hooke's tensor $c_{ijpq} = c_{ijqp}$, we have $F^{pq} = F^{qp}$, therefore $\chi^{pq} = \chi^{qp}$, and six elastostatic equations have to be solved in total to compute the corrector.

(ii) Step 2: build the fourth-order strain concentrator $\boldsymbol{G}$ as

$$G_{ijpq} = \frac{1}{2}\left(\delta_{ip} + \delta_{jq}\right) + \frac{1}{2}\left(\partial_i \chi_j^{pq} + \partial_j \chi_i^{pq}\right), \tag{15}$$

and the fourth-order stress concentrator $\boldsymbol{H} = \boldsymbol{c} : \boldsymbol{G}$, that is,

$$H_{ijkl} = \sum_{m=1}^{3}\sum_{n=1}^{3} c_{ijmn} G_{mnkl}. \tag{16}$$

(iii) Step 3: filter the concentrators $\boldsymbol{G}$ and $\boldsymbol{H}$ component by component so as to obtain $\boldsymbol{G}^{\varepsilon_0}$ and $\boldsymbol{H}^{\varepsilon_0}$ as

$$G_{ijkl}^{\varepsilon_0} = \mathscr{F}^{\varepsilon_0}\left(G_{ijkl}\right), \quad H_{ijkl}^{\varepsilon_0} = \mathscr{F}^{\varepsilon_0}\left(H_{ijkl}\right), \tag{17}$$

and build the equivalent effective elasticity tensor $\boldsymbol{c}^{*,\varepsilon_0}$ as $\boldsymbol{c}^{*,\varepsilon_0} = \boldsymbol{H}^{\varepsilon_0} : (\boldsymbol{G}^{\varepsilon_0})^{-1}$, that is,

$$c_{ijkl}^{*,\varepsilon_0} = \sum_{m=1}^{3}\sum_{n=1}^{3} H_{ijmn}^{\varepsilon_0} (G^{\varepsilon_0})_{mnkl}^{-1}, \tag{18}$$

where the inverse operation is to be understood in the algebra of fourth-order tensors.

Of note, the tensorial products in steps 2 and 3 are to be understood pointwise: it means that the corresponding algebraic operations are applied for each spatial position $\mathbf{x}$ independently. A final post-processing stage is applied to $\mathbf{c}^{*,\varepsilon_0}$ to guarantee the symmetry of the equivalent stiffness s tensor which is a physically required constraint. The final equivalent stiffness tensor is thus $\mathbf{c}_{\text{sym}}^{*,\varepsilon_0}$

$$\mathbf{c}_{\text{sym}}^{*,\varepsilon_0} = \frac{1}{2}\left(\mathbf{c}^{*,\varepsilon_0} + (\mathbf{c}^{*,\varepsilon_0})^T\right). \tag{19}$$

To simplify the notations, in the remainder of the study, we use the notation $\mathbf{c}^{*,\varepsilon_0}$ for $\mathbf{c}_{\text{sym}}^{*,\varepsilon_0}$.

Previous finite-element-like implementation of the non-periodic homogenization involves the following numerical strategies. A classical weak-form-based finite-element technique is used to solve the elastostatic equations and compute the concentrators χ^{pq}. The resulting finite-element discrete linear equation system of the elastostatic equation in step 1 is solved through a direct solver such as PARDISO (Schenk & Gärtner 2011) over distributed-memory

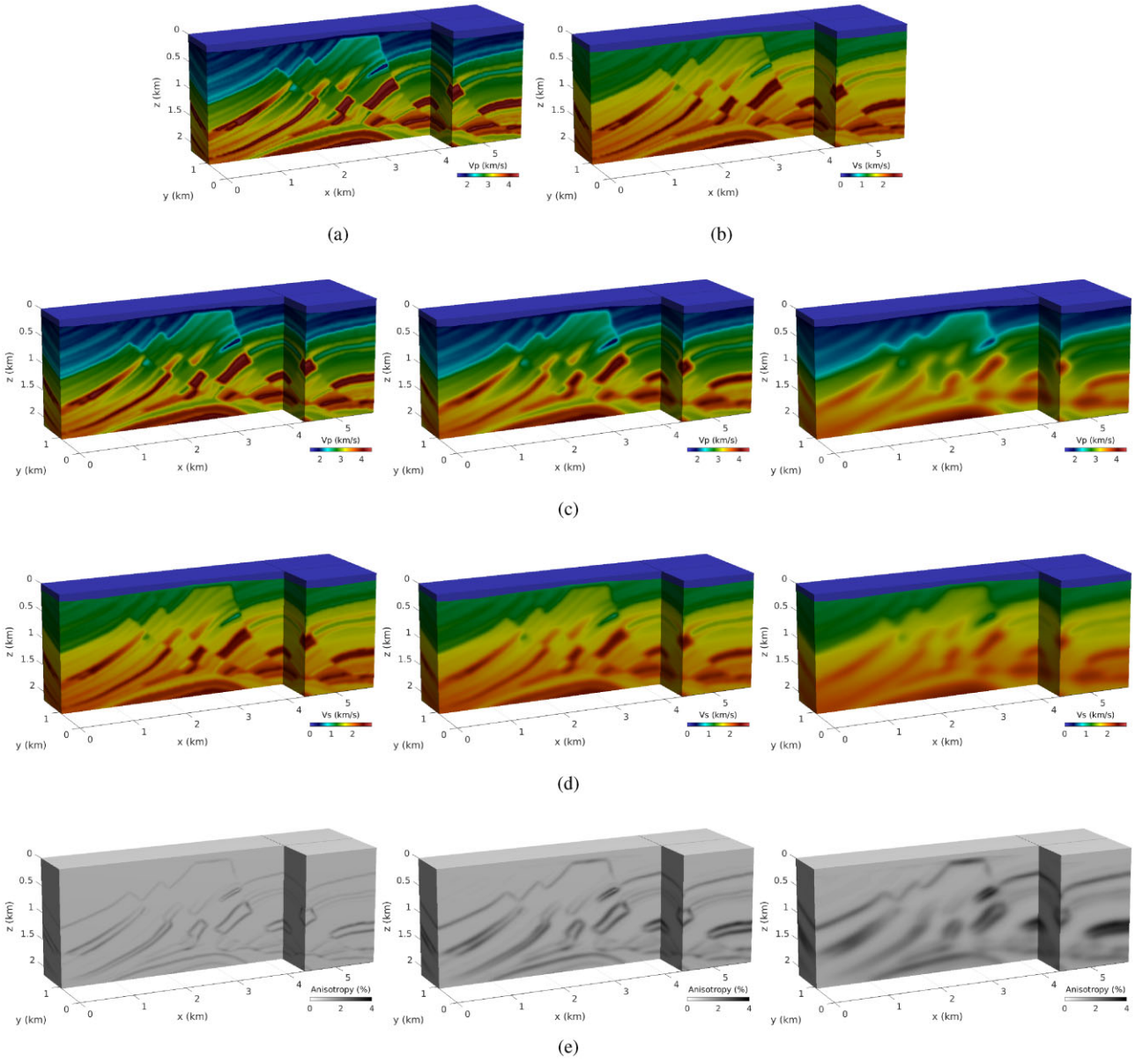

Figure 12. 3-D Marmousi-II marine velocity models and its effective models after the homogenization process. (a) and (b) are the original *P*-wave V_p and *S*-wave V_s velocity models. (c)–(e) are effective models of V_p, V_s and the total anisotropy in percentage obtained with $\varepsilon_0 = 0.2$, 0.4 and 0.8 from left to right, respectively. They are calculated by projecting the resulting elasticity tensor coefficients $\boldsymbol{c}^{*,\varepsilon_0}$ from the homogenization process to the closest isotropic model (Browaeys & Chevrot 2004).

platforms. This has the advantage to provide accurate solutions regardless of the conditioning of the discretized elastostatic equations. The main disadvantage of such strategy is the computational cost and memory imprint of direct solvers, and their lack of scalability. A recent study for the solution of frequency-domain 3-D elastodynamic equations illustrate this limitation (Li *et al.* 2020).

This issue is addressed in Cupillard & Capdeville (2018) where a domain-decomposition strategy is proposed, each subdomain being treated independently with a direct solver. Buffer layers are added to each of the subdomain as the solution is known to be invalid in a region of size λ_0 in the vicinity of the boundaries. The global solution is then built as a concatenation of the solution in each subdomain after removing the buffer layers. While applicable in practice, this solution lacks flexibility, and comes with a numerical over-cost that can be significant.

The implementation of step 2 is trivial, since it only involves algebraic tensor operations, for each gridpoint. Step 3 is the second key point: the low-pass filtering operation, as is going to be described further in the remainder of this study, is crucial. In current implementation, it is based on a Gaussian filter, with an explicit convolution process. While it can be efficiently applied on regular grids, it is much more computationally intensive on irregular or deformed grids, because of the extra interpolation operations to get the proper contribution points in the surrounding volume for each input point that needs to be filtered (Trinh *et al.* 2017).

In this study, we propose an integrated method which overcomes the aforementioned limitations. It works on the same GLL mesh used to solve the elastodynamics equations with the SEM, therefore avoiding any interpolation/extrapolation step on a regular grid, and it exploits the similarity of the computational kernels

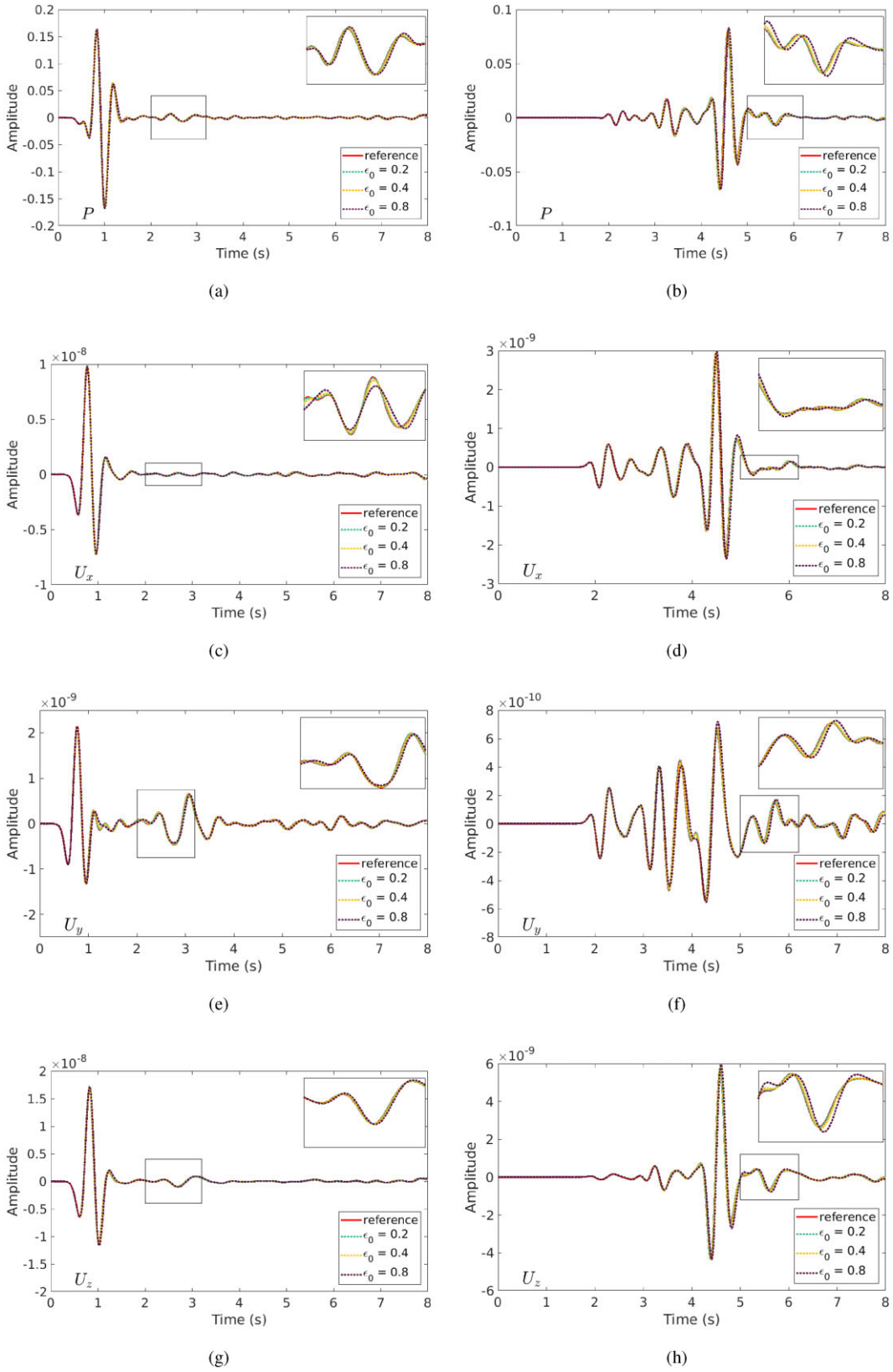

Figure 13. Seismogram comparison of the 4C OBN data (pressure wavefield and 3C displacement wavefield on the seabed) computed at the receivers of (a), (c), (e) and (g) the near offset $x = 320$ m and (b), (d), (f) and (h) the far offset $x = 3200$ m. The homogenized solutions with different ε_0 are benchmarked again the reference solution (red line) which is generated from the original model. An excellent agreement is obtained when $\varepsilon_0 = 0.2$, since the green dashed lines (the homogenized solution with $\varepsilon_0 = 0.2$) almost fully cover the red solid lines (the reference solution). Here, the wave simulation is performed by using a fluid–solid coupled SEM solver (Cao *et al.* 2022b).

among the elastodynamics equations, the elastostatic equations and the Bessel filtering equations to provide an efficient and domain-decomposition-based scalable algorithm. We present this method in Section 3.

3 FULLY SCALABLE IMPLEMENTATION OF THE 3-D NON-PERIODIC HOMOGENIZATION

3.1 Similarity of the equations

The similarity between the elastodynamic and elastostatic equations is clear from equations (13) and (14). The latter is the same as the former minus the dynamics part related to the second-order partial derivatives in time of the displacement field u. The Bessel filtering we are going to use for the step 3 in the homogenization process also shares similarities with these equations. More precisely, giving an input model $m(\mathbf{x})$, the filtered version $s(\mathbf{x}) = \left(\mathscr{F}^B(m)\right)(\mathbf{x})$ is obtained by solving the equation

$$s - \sum_{j=1}^{3} l_j^2 \partial_j s = m, \tag{20}$$

where l_j are associated with correlation length in direction j to design an anisotropic (possibly non-stationary) filter (see the details in Trinh *et al.* 2017). Eq. (20) can be seen as a (strongly) simplified version of the elastodynamic equations with the following identification

$$\partial_{tt} u \longleftrightarrow s, \quad c_{ijkl} \longleftrightarrow l_j^2. \tag{21}$$

This analogy provides us with the possibility to use the same finite-element formalism to compute numerical approximation of the solutions of all these equations.

We make use of the SEM, which is a standard in seismology since the seminal work of Komatitsch (1997) and Komatitsch & Vilotte (1998). This discretization method is based on the use of Lagrange polynomial on hexahedral elements, and GLL points for the quadrature rules. Choosing the same collocation and integration point yields a diagonal mass matrix M, while the GLL points have the interesting properties to position points at the boundaries of the elements, making it possible to enforce directly the continuity of the field between elements without any additional constraints. Choosing these points also ensure spectral convergence, the property which initiated the interest of such strategies when they were conceived (Patera 1984). Interestingly, this is not the main reason the method has become popular in seismology. The success of this method in this field is more related to its excellent numerical dispersion properties, which makes it possible to use fewer points to sample the wavefield compared with finite-difference strategies in the context of the elastic approximation and the propagation of surface waves. The fact that the mass matrix is diagonal is also a strong point compared to conventional finite-element strategies: when using explicit time schemes, no matrix inversion is required. Finally, as it is a finite-element based method, it is possible to work with deformed meshes to conform to specific geometries, and the free surface condition is inherently taken into account thanks to the weak form of the equations which is solved. The latter is a strong advantage over finite-difference methods, which require specific treatment for handling the free surface boundary condition as soon as the free surface boundary is not flat.

Following the SEM strategy, the corresponding semi-discrete elastodynamics equations can be written as

$$\mathbf{M}\partial_{tt}\mathbf{u} - \mathbf{K}\mathbf{u} = \mathbf{b}, \tag{22}$$

where $\mathbf{M}$ is the diagonal mass matrix and $\mathbf{K}$ is the so-called stiffness matrix. Using a second-order explicit time scheme, solving the elastodynamics equations amount to compute $\mathbf{u}^n$ from $\mathbf{u}^0$ as

$$\mathbf{u}^{n+1} = 2\mathbf{u}^n - \mathbf{u}^{n-1} + \frac{1}{\Delta t^2}\mathbf{M}^{-1}\mathbf{K}\mathbf{u}^n + \frac{1}{\Delta t^2}\mathbf{M}^{-1}\mathbf{b}^n. \tag{23}$$

In practice other explicit time schemes are often employed, namely the Newmark's scheme tends to be a reference. As it is not the main focus of the study we choose this simple second-order finite-difference time scheme for the sake of clarity.

From eq. (23), we see that the matrix $\mathbf{K}$ is the key kernel in the implementation of the SEM method for the solution of elastodynamics equations. Indeed, the operator $\mathbf{M}$ being diagonal, the application of its inverse has the complexity of a scalar product, while the operator $\mathbf{K}$ is a sparse operator with a sparsity pattern associated with the mesh and the chosen polynomial degree of the Lagrange interpolants.

In the development of the code SEM46, we have come to a very efficient and scalable implementation of the matrix-vector product $\mathbf{Ku}$, relying on loop unrolling, cache optimization, vectorization and domain decomposition, up to the use of several thousands of computing units (Deville *et al.* 2002; Trinh *et al.* 2019; Cao *et al.* 2022a, b; Tarayoun *et al.* 2022). We rely on fourth- and fifth-order Lagrange polynomial, which gives a good trade-off between numerical dispersion property and smallest distance between two adjacent discretization point, the latter governing the stability constraint of the explicit-time scheme (also known as CFL condition).

Using the same discrete formalism, the elastostatic equations can be written as

$$-\mathbf{K}\chi^{pq} = \mathbf{F}^{pq}, \quad p = 1, \ldots 3, \quad q = p, \ldots, 3. \tag{24}$$

The Bessel filtering equations can be written as

$$\mathbf{s} - \mathbf{K}^{\text{Bessel}}\mathbf{s} = \mathbf{m}, \tag{25}$$

or equivalently

$$\left(\mathbf{I} - \mathbf{K}^{\text{Bessel}}\right)\mathbf{s} = \mathbf{m}, \tag{26}$$

with $\mathbf{I}$ the identity operator and $\mathbf{K}^{\text{Bessel}}$ a simplified version of the SEM kernel $\mathbf{K}$ which shares a similar structure. Eqs (23), (24) and (26) reveal the link among elastodynamics equations, elastostatic equations and Bessel filtering equations, and emphasize the importance of the stiffness matrix $\mathbf{K}$.

Contrary to the elastodynamic equations which rely on an explicit scheme, both the elastostatic equations and the Bessel filtering operation turn to the solution of linear systems. We describe in the next paragraph how we can solve these linear systems using a matrix-free conjugate gradient algorithm, which exploits the optimized matrix-vector product $\mathbf{Ku}$ implemented in the SEM46 code.

3.2 The elastostatic equation solution with conjugate-gradient method

The motivation to use a conjugate gradient algorithm (Hestenes & Stiefel 1952) to solve the system (24) has been already stated: it overcomes the memory limitation from direct solvers as well as their lack of scalability. Only the matrix-vector product operation is required, which is already available, optimized and

scalable through a matrix-free implementation and a domain decomposition algorithm.

What remains to be ensured is the convergence of such an iterative solver. The matrix $\mathbf{K}$ comes from the discretization of a generalized Helmholtz operator, therefore it is a symmetric positive operator. However, depending on the boundary conditions, it might have a non-empty kernel preventing the convergence of the conjugate gradient algorithm (see, for instance, Tang *et al.* 2022, where a similar linear system is solved in the frame of a controllability method for computing the frequency-domain solution of the elastodynamics equations). This is the reason why instead of periodic boundary conditions, we impose on purpose Dirichlet boundary conditions, making the operator $\mathbf{K}$ symmetric positive definite. This has an effect to generate a spurious solution in a thin layer at the model boundaries, as observed and documented in Capdeville *et al.* (2015), where the same boundary condition is used. The width of this layer is apparently to the order of λ_0. Numerical experiments show that the error on the solution remain confined in this thin layer, with no influence in the inner part of the domain. This complies with the fact that the boundary condition effect decays exponentially in the elastostatic equation. The pragmatic solution we implement is thus to add buffer layers around the model, similar as what is done for the elastodynamics equations when using sponge layers to attenuate outgoing waves.

To speed-up the convergence of the conjugate gradient algorithm, we also make use of a pre-conditioner. The latter is simple: relying on a Jacobi strategy, we simply extract the diagonal of the operator $\mathbf{K}$ and take its inverse as a pre-conditioner $\mathbf{P}$, such that

$$\mathbf{P} = (\mathrm{diag}\,(\mathbf{K}))^{-1}\,. \tag{27}$$

As shown in Fig. 2 for the test on a 3-D random model (which is detailed in Section 4.1), this pre-conditioner is already quite efficient and makes it possible to accelerate the convergence by factors of more than 5 to reach a relative-residual level of 1.E-3 and 2 to reach a relative-residual level of 1.E-5. In addition, by comparing the convergence curves among two different meshes, we can also observe that this acceleration turns out to be more efficient as the problem size increases.

We summarize this section by presenting the algorithm implemented to solve the six elastostatic systems (24) in Table 1.

3.3 Low-pass filter design

The step 3 of the homogenization process requires to apply a low-pass filter to remove scales smaller than $\lambda_0 = \varepsilon_0 \lambda_{\min}$ from the concentrators ($\mathbf{G}$) and ($\mathbf{H}$). The ideal filter to perform this operation should have a boxcar response in the wavenumber domain. However, in practice, implementing such an ideal filter is difficult. In Fig. 3, three examples of filters are presented: the cosine taper filter with the closest response to the ideal filter, the Gaussian filter, which is conventionally used for homogenization, and the Bessel filter we consider in this study. In practice, the Gaussian filter is used because of its compact wavelet and absence of negative amplitude responses. Such a negative amplitude, which we observe with the cosine filter for instance, would create instability issues during the convolution with highly heterogeneous fields. The problem with Gaussian filter has been denoted previously: to be implemented it requires a projection on a Cartesian grid, which results in loss of accuracy and degraded numerical efficiency. This is the reason why we are interested in the Bessel filter, which can share the same numerical framework as the elastodynamics and elastostatic problems thanks to the general PDE formalism on which it relies.

Solving directly the Bessel equation (26) avoids any projection as it is posed directly on the SEM mesh. The same CG algorithm 1 is thus used to solve the Bessel equation and apply the filter, replacing $-\mathbf{K}$ with $I - \mathbf{K}^{\mathrm{Bessel}}$. The addition of the identity matrix also improves the conditioning of the system and makes it possible to choose Neumann boundary condition instead of Dirichlet boundary conditions.

There is however one difficulty which is posed by the use of the Bessel's filter. We can usually approximate a Laplace filter by cascading two Bessel filters (Fig. 3; Trinh *et al.* 2017). However, as illustrated in Fig. 3(b), the Laplace filter exhibits a suboptimal steep response for homogenization. From this perspective, the Gaussian filter exhibits a better wavenumber response, closer from the steep boxcar ideal filter we want to approximate. However, thanks to the central limit theorem, it is possible to replicate a Gaussian-like response through a cascade of filters (Wells 1986). To do so, we propose to calibrate the Bessel's filter with a specific stretching factor α, such that the filter $\mathscr{F}^B_\alpha(m)$ is given by the solution of

$$\left(I - \alpha \sum_{j=1}^{3} l_j^2 \partial_j\right) s = m. \tag{28}$$

The cascade of filters we consider is $\mathscr{F}^{B,n}_\alpha$ defined as the n-times composition of the filter $\mathscr{F}^B_\alpha$

$$\mathscr{F}^{B,n}_\alpha = \underbrace{\mathscr{F}^B_\alpha \circ \cdots \circ \mathscr{F}^B_\alpha}_{n \text{ times}}. \tag{29}$$

It should be noted that the stretching factor α is case independent, therefore this calibration step does not add any computational overhead or complexity to the homogenization recipe we are proposing. The computation of the values of α and n, we present in the following, can be readily used for any application.

In order to solve for the optimal values of α and n, we define a minimization problem as

$$\arg\min_{\alpha,n} \; [1 - \mathrm{Corr}(\mathscr{G}^0, |\mathcal{F}[\mathscr{F}^{B,n}_\alpha(\delta)]|), \tag{30}$$

which is nothing else than maximizing the correlation coefficient between the sought analytical Gaussian filter wavenumber response $\mathscr{G}^0$ (Fig. 4a, the red solid line) and the calculated response of the cascaded custom filter $r_{cal} = |\mathcal{F}[\mathscr{F}^{B,n}_\alpha(\delta)]|$ (Fig. 4a, dashed lines). In practice, the latter wavenumber domain response is obtained by performing a 3-D discrete Fourier transform of the impulse response and deducing the amplitude of the spectrum.

The 2-D real-integer problem related to finding the optimal real value of α defined in the spatial domain and the acceptable number of Bessel filter application n described in eq. (30) is convex along the real dimension for all values of α where $\mathscr{F}^{B,n}_\alpha$ is defined. In practice, the problem is split and the optimization is done for a range of n as illustrated in Fig. 4(a) for $n = 1$ to 10. It should be noted that for this particular problem, according to the central limit theorem, as n increases, the impulse response of the cascaded filter tends towards the sought impulse response of the Gaussian filter so there is no need to actually solve the 2-D real-integer problem as long as the optimal stretching factor α is found for a suitable and practical number of Bessel filter application.

The optimization for α is done using a classical implementation of particle swarm optimization (PSO) algorithm (Kennedy & Eberhart 1995) with both cognitive and social coefficients set at 0.1 and a fixed inertia weight of 0.8. The values of α are bounded between 10^{-5} and 0.5 using a random boundary condition. We opted for PSO, knowing that the problem at hand is convex, and the method is

derivative-free, insensitive to parameter scaling and generally more efficient than grid-search strategies or other global optimizers. The results presented in Figs 4(a) and (b) show the spectra and misfit values for different values of α and number of applications of the filter are presented and as expected, increasing the number of Bessel filters yields more accurate approximation of the Gaussian filter. As an example, in Fig. 4(a) (orange fine dashed line), for $n = 10$ and its corresponding optimal stretching factor, the response correlates the most with the Gaussian response (Fig. 4a, red solid line). Having said that we remind the reader that the global minimum of the function defined by eq. (30) is at theoretical convergence where $\lim_{\substack{n\to\infty \\ \alpha\to 0}} \mathscr{F}_{\alpha}^{\mathcal{B},n}$.

In practice, we consider a trade-off between accuracy and computational cost as shown in the graph superposition of Fig. 4(c). Since the optimal stretching factor decreases as the number of filter application increases we see that the computational cost does not grow in a linear fashion with n. The latter is a good property that enables choosing practical optimal values even at an increased number of Bessel filtering application. We recommend and use across the paper a stretching factor of $\alpha = 6.496 \times 10^{-2}$ at $n = 4$ or alternatively $\alpha = 5.752 \times 10^{-2}$ with $n = 5$ which corresponds to the intersection of the two curves of Fig. 4(c). The latter parameter tuning, tested throughout our implementation of the proposed strategy, is a fair compromise between accuracy and cost for problems of the size and type found in seismic modelling.

4 APPLICATIONS

In this section, we illustrate the interest of our homogenization implementation to upscale large 3-D elastic models. We start with a validation test in a 3-D random elastic medium for which we can test the convergence of our homogenization algorithm. Next, we consider the entire 3-D SEAM II foothill model to investigate the feasibility of our proposed homogenization method in a large-scale onshore exploration context. Thanks to the scalability and the flexibility of our implementation, we manage to homogenize an unprecedented large-scale model containing almost 15 billions of discrete unknowns. We repeat a similar experiment in an offshore exploration context, using a 3-D extension of the Marmousi-II model. Since no theoretical results exist for upscaling fluid/solid coupled media, we propose a pragmatic approach where only the solid part is homogenized, leaving the fluid layer untouched. The numerical results we obtain are convincing: such strategy might be used to decrease the computational cost of modelling in such fluid/solid media. In all the presented experiments, we use a fourth-order Lagrange polynomial spectral-element discretization.

4.1 Validation tests on a 3-D random model

We consider a highly heterogeneous isotropic medium in a cubic domain of 15 km^3 made of a constant background, where the pressure wave velocity V_p, the shear wave velocity V_s and the density ρ are

$$V_p = 5000\ \mathrm{m\,s^{-1}}, \quad V_s = 3200\ \mathrm{m\,s^{-1}}, \quad \rho = 3000\ \mathrm{kg\,m^{-3}}, \tag{31}$$

and randomly distributed cubic inclusions of 100 m^3 scale, where V_p, V_s and ρ values differ from ± 50 *per cent* from the background. The instance of such random medium we consider in this study is presented in Fig. 5(a). We consider the propagation of a wavefield generated by a vertical force source localized in the centre of the domain, emitting a 1.6 Hz Ricker wavelet. The maximum frequency is approximately $f_{\max} = 4$ Hz. The minimal wavelength $\lambda_{\min}$ we consider for the filter design is based on the shear wave velocity value in the background $V_s = 3200\ \mathrm{m\,s^{-1}}$ and this maximal frequency, giving $\lambda_{\min} = 800$ m, meaning that we have eight cubic inclusions per $\lambda_{\min}$ in each Cartesian direction.

We present in Fig. 5(b), the equivalent media from our homogenization algorithm corresponding to the choice $\varepsilon_0 = 1.0$. Since its equivalent stiffness tensor $\boldsymbol{c}^{*,\varepsilon_0}$ is fully anisotropic, more precisely, we present the resulting effective 'vertical' V_p^{*,ε_0} model,

$$V_p^{*,\varepsilon_0} = \sqrt{\frac{c^{*,\varepsilon_0}_{3333}}{\rho^{*,\varepsilon_0}}}, \tag{32}$$

implying any heterogeneities below the minimal wavelength are considered as apparent anisotropy.

In Figs 5(c)–(e), we compare the wavefields computed in the equivalent media with the ones computed in the reference isotropic fine-scale medium in terms of wavefield snapshots and shot gathers. We can see the effective solution exhibits an excellent agreement with the reference wavefield regarding the propagation of transmitted energy, both in terms of traveltimes and amplitude. On the other hand, the weak-amplitude scattered field is less well approximated as expected, since more discontinuities are filtered out in the low-pass filtering step: a smaller value of ε_0 would improve this.

Besides this qualitative first analysis, we perform a quantitative convergence study where we homogenize this 3-D model for different values of ε_0 ranging from 0.1 to 1.0. In Fig. 6(a), 1-D depth profiles extracted in the middle of the resulting effective 'vertical' V_p^{*,ε_0} models are presented. We can see, as expected, that less and less small-scales heterogeneities are preserved in the homogenization process. For each value of ε_0, we compute the relative error between the exact wavefield and the one computed in the corresponding equivalent medium, as presented in Fig. 6(b). To be more precise, the exact wavefield is the one computed in the original medium with a fine mesh based on 100 m^3 cubic elements (the size of the cubic heterogeneities). The approximate wavefields are the wavefields computed in the equivalent media on the same fine mesh. Doing so, we do not bias the error estimation by a second source of error coming from a coarser discretization. Of course, in practice, we would use indeed coarse meshes as the intent of such homogenization is ultimately to decrease the computational cost. The experiment here is a validation test to quantify the convergence rate of the numerical homogenization strategy we deploy.

Although Capdeville *et al.* (2010b) demonstrate that the homogenized wavefield solution converges asymptotically towards the reference wavefield solution (generated from the original medium) with a $O\left(\varepsilon_0^2\right)$ convergence rate, Fig. 6(b) shows that we actually obtain a convergence order between $O(\varepsilon_0)$ to $O\left(\varepsilon_0^2\right)$ (see the dash lines between the two red lines). The latter is due to two reasons. First, we do not implement an effective source as mentioned in Section 2.1. In the worst case, this can bound the convergence error to $O(\varepsilon_0)$. Second, it is due to the fact that the filter used to low-pass filter the concentrators has a biased wavenumber response compared with an ideal boxcar-type filter considered in the optimal case for the mathematical demonstration. We also compare in Fig. 6(b), the convergence depending on the choice of the Bessel-based low-pass filter: one where 4 Bessel's filters are used with $\alpha = 6.496 \times 10^{-2}$, one where 5 Bessel's filters are used with $\alpha = 5.752 \times 10^{-2}$. The two results are almost equivalent, indicating a robustness with respect to these parameters. This test is also an opportunity to compare the behaviour of our cascaded Bessel's filter strategy with

the use of a Gaussian filter, by paying the price of an explicit convolution with a true Gaussian-filter wavelet in the homogenization process as shown in Fig. 6(b). The accuracy of the homogenized solution obtained with the cascaded Bessel's filter is similar to the one corresponding to the Gaussian filter, and is even superior at low ε_0, owing to its PDE-based implementation that preserves the SEM precision consistency of all the homogenization steps. This higher accuracy of the Bessel-based homogenization for small ε_0 might be due to the way we implement the Gaussian filtering here: to work on the Gauss-Lobatto-Legendre (GLL) point, we have to interpolate model parameters in the 3-D volumes built to window the Gaussian convolution. This interpolation might tend to be less accurate when the model heterogeneities are smaller, which is the case when ε_0 decreases.

We finalize this first test by analysing the performance of our algorithm in terms of scalability and high performance computing. First we give in Table 2 the size of the model, the number of iterations performed to solve the elastostatic problems and to filter the concentrators, and the total elapsed time on 960 CPU cores. In average, around 1500 CG iterations are required to solve each of the 6 elastostatic problems, while less than 800 are required to apply the cascaded Bessel's filter. The size of the model is already significant with 161 elements in each direction, leading to a 810 million degrees of freedom (DOF) size problem.

Second we present a strong scalability test, where we measure the reduction in elapsed time of the whole homogenization process when the number of CPU cores increases. We consider running the same homogenization process with two different meshes: one with 128^3 elements (410 million DOF), and the second with 256^3 elements (3.24 billion DOF). We set ε_0 to 0.5 in these two cases, which correspond to the half-wavelength resolution usually considered for seismic imaging. We observe for the two meshes a quasi-perfect linear scalability for a number of CPU cores going from 240 to 1920. For the larger mesh, the memory requirement for solving each elastostatic equation is too big to be run on a single node, hence the absence of result in this case (first point is missing). The scalability test is illustrated in Fig. 7, and for more details, the corresponding numbers are given in Table 3.

4.2 3-D SEAM-II foothill model

Next we consider a more realistic large-scale onshore model: the 3-D SEAM-II benchmark foothill model. This model was designed to represent challenges of seismic exploration in mountainous regions, especially for rough topography of mountain regions interacting with strong lateral variation in the first few hundred metres of the subsurface. More details on this model and the SEAM project can be found in Oristaglio (2012). From the perspective of elastic wavefield modelling, such a model is very challenging. The deformation of the mesh to conform to the rough topography leads to the creation of elongated elements, as shown in Fig. 8.

Figs 9(a)–(c) present the corresponding *P*-wave velocity V_p, *S*-wave velocity V_s and density ρ models. To model accurately the wavefield propagating in this medium, the presence of fine-scale structures and heterogeneities requires to decrease the element size down to $\lambda_h = 30$ m. For a model of size 9.87 km $\times$ 14.46 km $\times$ 12.48 km, this discretization leads to 339 $\times$ 502 $\times$ 436 elements in *z*-, *x*- and *y*- directions, respectively (including 10 sponge-layer elements on each side, except for the top where the free-surface boundary condition is applied, for attenuating outgoing wave and prevent from spurious reflections). According to the fourth-order Lagrange interpolation we use, this leads to $(339 \times 4 + 1) \times (502 \times 4 + 1) \times (436 \times 4 + 1) \times 3 \simeq 14.27$ billion DOF. However, if we consider simulating the wave propagation induced by a vertical force localized in the middle of the free surface at $x = 7230$ m, $y = 6240$ m, with a 2 Hz Ricker wavelet ($f_{\max} = 5$ Hz) as source time function, the minimum wavelength to consider is $\lambda_{\min} = 127.98$ m much larger than the smallest heterogeneity: $\lambda_{\min} \gg \lambda_h$. This makes this example ideal for showing the practical benefits provided by homogenization in terms of computation cost reduction for seismic wave modelling.

We apply the proposed CG-based homogenization process to this model with scaling parameters $\varepsilon = 0.25$, 0.5 and 1.0, respectively. Since we achieve a similar accuracy in the homogenized solutions by using the cascade of 4- and 5-times Bessel filters in the previous case, we here choose 4-times Bessel filter which is slightly less computationally demanding. Two particular points need to be taken into consideration:

(i) potential site effects at the near surface;
(ii) the use of a variable local minimum wavelength $\lambda_{\min}$.

Regarding the first point, it is explained in Capdeville & Marigo (2008, 2013) that when computing the wavefield at the surface, a first-order correction should be considered in the homogenization approximation, to take into account the presence of shallow heterogeneities and specific site effects. The computation of this first-order correction is however cumbersome, and goes beyond the scope of this study. A pragmatic approximation of the first-order correction consists of mirroring the medium parameters with respect to the surface topography along the local normal to the topography (Capdeville & Marigo 2007), so as to fill-in the buffer layer on top of the surface. This strategy shows to be efficient in the following numerical experiments. The second point is related to the possibility to use a single value for ε_0 in the whole medium, while the minimum wavelength varies within the medium due to the variation of velocities (see Capdeville *et al.* 2013, appendix B). To account for these variations, we define a spatially varying $\lambda_{\min}(\mathbf{x})$ as

$$\lambda_{\min}(\mathbf{x}) = \frac{V_s(\mathbf{x})}{f_{\max}}, \tag{33}$$

and define accordingly $\lambda_0(\mathbf{x})$ as

$$\lambda_0(\mathbf{x}) = \varepsilon_0 \lambda_{\min}(\mathbf{x}). \tag{34}$$

This spatially varying coherence length can be taken into account naturally by the Bessel filter we use.

We present in Fig. 9 the effective models obtained for the three different values of ε_0 we consider, namely $\varepsilon_0 = 0.25$, 0.5 and 1. These models are the projection of the equivalent stiffness tensor $\boldsymbol{c}^{*,\varepsilon_0}$ to the nearest isotropic V_p and V_s models (its stiffness tensor is represented as $\boldsymbol{c}^{*,\varepsilon_0}_{\text{iso}}$), following the work of Browaeys & Chevrot (2004). The percentage of anisotropy in $\boldsymbol{c}^{*,\varepsilon_0}$ is computed as

$$\text{Anisotropy}\,(\mathbf{x}) = \frac{\sqrt{\sum_{ijkl}\left(c^{*,\varepsilon_0}_{\text{iso},ijkl}(\mathbf{x}) - c^{*,\varepsilon_0}_{ijkl}(\mathbf{x})\right)^2}}{\sqrt{\sum_{ijkl}\left(c^{*,\varepsilon_0}_{\text{iso},ijkl}(\mathbf{x})\right)^2}}. \tag{35}$$

We observe a significant apparent anisotropy behaving like a locally tilted transverse isotropy. The percentage of anisotropy increases with ε_0 to compensate the small-scale contrasts missing in V_p and V_s models, which is consistent with the homogenization theory. The discretization details and the associated computational cost of the proposed homogenization process using $\varepsilon_0 = 0.5$ are given in

Table 4. We see that the size of the problem reaches 14.69 billion DOF. Using 7680 CPU cores, the total elapsed time for the homogenization is approximately 3 hr, the number of CG iterations for the elastostatic problems is around 13 000, and less than 420 for the low-pass filtering part.

We perform a modelling test in the model corresponding to $\varepsilon_0 = 0.5$. We compare three wavefields: the wavefield computed in the reference model using the fine mesh with 30 m element size, the wavefield computed in the equivalent model using the same fine mesh, and finally the wavefield computed in the equivalent model using a coarse mesh whose elements size are adapted to the local V_s velocity (estimated by projecting the homogenized tensor $\boldsymbol{c}^{*,\varepsilon_0}$ to the nearest V_s model). The result of this experiment is presented in Fig. 10. For each component u_x, u_y and u_z we display the reference wavefield at the free surface at time $t = 3.725$ s, and in-line and cross-line traces where we compare the three wavefields. One can appreciate the excellent match between the three wavefields, both in terms of amplitude and phase, indicating the efficiency of the homogenization strategy in this case. A further comparison in terms of shot gather is shown in Fig. 11, which quantitatively reveals that the relative difference between the seismic data modelled from the dense-mesh discretized original model and the seismic data modelled from the adaptive coarse-mesh discretized equivalent model is less than 1.6 percentage.

The statistics of the modelling test are presented in Table 5. The total number of elements is divided by approximately a factor 90, while the number of time-steps is divided by a factor 5. This reduction of the number of time-steps results from the use of a coarser mesh which leads to a less constrained CFL stability condition for the explicit time-marching scheme. The modelling on the fine mesh is performed in 98 min on 2560 CPU cores. The modelling on the coarse mesh is achieved in 5.2 min on 160 CPU cores. In terms of total CPU hours (elapsed time when using a single CPU core, which quantifies the computational complexity) this represents a reduction of a factor 300, which is very significant. This is an illustration of what can be expected in terms of computation cost reduction from the use of homogenization theory in this context. Of note, there is a computational kernel optimization in the fine-scale isotropic case so as to take into account the specific sparsity of the stiffness tensor $\boldsymbol{c}$ in this case, however, in the equivalent medium, a fully populated $\boldsymbol{c}$ stiffness tensor is taken into account. This kernel optimization does not compensate, by far, the computational cost difference induced by the possibility to use a coarser mesh from the equivalent medium.

To complement this modelling cost comparison, it should be noted that the extra cost of homogenization process for getting the effective model also needs to be taken into account. In this experiment, the elapsed time for homogenization is around 3 hr using 7680 CPU cores, which is apparently more expensive than performing the modelling directly on the fine mesh (1.63-hr elapsed time using 2560 CPU cores). If we compare these two costs in terms of total CPU time, the homogenization process is about 5.5 times as much as a direct modelling on the fine mesh. Thus, for a one-time seismic modelling, it is not worthy of using the homogenization strategy in this case. However, most of 3-D seismic applications require solving the modelling problem for hundreds to thousands of sources, for instance in Full Waveform Inversion (FWI, Virieux *et al.* 2017). Here, starting at five different sources, it becomes more interesting to use the homogenization strategy. Let us stress that this number is case-dependent: depending on the roughness of the heterogeneities, the maximum frequency of the signal, there might be situations for which homogenization is not interesting before a very large number of modelling is required, and others for which homogenization is already interesting for a single source.

4.3 3-D Marmousi-II marine model

To finalize this study, we consider here a realistic offshore problem based on a 3-D extension of the Marmousi-II model (Martin *et al.* 2006). It is a simple extension along the y-direction with an angle of 45°, and an uneven seabed is added to replace the original flat one. The model is presented in Figs 12(a) and (b). Given the ongoing importance of the deployment of ocean bottom seismometers (OBS) for imaging the crust at exploration and lithospheric scales, it is important to assess if the homogenization tools we propose can be used in such a context. In general, similarly to the free surface, homogenization cannot remove solid–fluid large interfaces. Small fluid inclusions can be homogenized and replaced by a solid (see Capdeville *et al.* 2020, p. 280 for an example), but this is the only case for which such a solution is possible. Solid–fluid interface topography can be homogenized in the same way as for the free surface topography (Capdeville & Marigo 2013), then replacing a rough topography by a smooth topography to the leading order, and changing the coupling conditions to the next order. In the same way as for the previous example, here we remain at the leading homogenization order. In practice, this means taking a pragmatic approach where the elastic part is homogenized independently from the fluid layer, and the equivalent fluid–solid model is built by adding the fluid layer on top of the equivalent elastic medium. As in the previous example, we consider a point vertical force source emitting a 2 Hz Ricker wavelet, located in the water layer. The maximum frequency $f_{\max}$ is thus $f_{\max} = 5$ Hz as for the previous experiment on the SEAM II Foothill model. We also consider a λ_0 adapted to the local minimum wavelength (equation 34).

Figs 12(c)–(e) display the resulting anisotropic equivalent models with scaling parameters $\varepsilon_0 = 0.2$, 0.4 and 0.8 projected to their nearest isotropic V_p, V_s models and the remaining total anisotropy percentages computed following eq. (35). As for the previous case, through the remaining total anisotropy percentages, we can observe its amount increasing with ε_0, which is expected from the homogenization theory: small-scale heterogeneities are seen as an equivalent anisotropy. In order to account for the effect of the fluid–solid interface in the seismic modelling, we adopt a fluid–solid coupled modelling engine in which the fluid and solid domains are divided explicitly and handled with the acoustic wave and elastic wave equation, respectively. The mutual interaction between these two wave equations is modelled by specific fluid–solid boundary conditions. This strategy is described in details in Cao *et al.* (2022b).

In Fig. 13, we present synthetic seismograms corresponding to two 4-component (4C) OBS recording the pressure and the particle 3C displacement in the near offset (320 m away from the source) and far offset (3200 m away from the source). These synthetic seismograms are computed both in the reference medium and the equivalent medium for the different values of ε_0 mentioned above. We can observe again a very good agreement between these seismograms in all cases, and the convergence towards the reference solution for decreasing values of ε_0 qualitatively. This experiment suggests that, despite the homogenization theory is not developed for a fluid–solid elastic medium, the pragmatic approach we propose, namely separating the fluid and solid parts and homogenizing the solid part before merging them to be a candidate homogenized model, might provide a first answer to the question of how to upscale a coupled fluid–solid medium.

5 CONCLUSION AND PERSPECTIVES

In this study we review the process of homogenization and propose an efficient numerical strategy to upscale large-scale 3-D elastic media. The main idea of our method comes from the identification of relevant mathematical analogy among the system of elastodynamics equations, the elastostatic equations and the filtering operations, the latter two being at the core of the homogenization process. All these equations are based on partial differential equations sharing the same spatial derivative operator. Because of this similarity, we can re-use the optimized numerical kernel developed for elastodynamics equations, based on a spectral-element discretization and a domain decomposition algorithm, to obtain a fully scalable, optimized, and matrix-free homogenization process.

We validate our approach on a 3-D random medium where we can test the convergence of the homogenization process, before we consider a realistic large-scale 3-D elastic model representing an onshore exploration project in foothill environments. We illustrate the scalability of our method and its capability to handle a problem involving around 15 billions of unknowns using several thousands of computing units. Based on this problem, we illustrate the interest of the homogenization method to model complex wavefields in onshore foothill environment. With a controlled accuracy, we can reduce the computation cost, in terms of total CPU hours, by a factor of 300. This is due to the fact that compared to the isotropic fine-scale model which requires small elements to represent small-scale heterogeneities, its homogenized counterpart is fully anisotropic and smooth, making it possible to use a much coarser mesh to model the elastic wavefield propagating in it.

This computational speed-up however needs to consider the computational effort needed to obtain the equivalent media by solving the homogenization problem. For single-shot modelling the gain might not be noteworthy as the 3-D homogenization problem represents itself a heavy problem. In terms of computational complexity, the elastostatic and Bessel's smoothing operation scales as a power 3 of the number of points in one dimension times the number of iterations to solve the corresponding linear systems. Depending on the number of iterations, it can be comparable to the solution of the elastodynamics equations, even if this number of iterations seems less constrained than the number of time-steps resulting from the CFL condition for time-dependent wavefield. In any case, as long as multiple simulations have to be performed in the same model, whether it is for inversion, sensitivity analysis, or wavefield amplification assessment, the homogenization strategy becomes interesting. The homogenization has to be solved only once, and all the wave propagation modelling then benefit from the reduction coming from the usage of a coarser mesh.

We complement our numerical study by investigating the question on how to homogenize fluid–solid coupled media. We propose a pragmatic approach where the elastic part is homogenized separately before being merged back with the fluid layer on the top of it. Despite lacking of the rigorous theory support of homogenization, this approach appears numerically accurate for the 3-D extended Marmousi II model we consider.

From the perspective point of view, we will focus on the application of this strategy in the frame of Full Waveform Inversion (FWI), in the continuity of the preliminary work presented in Capdeville & Métivier (2018), with several questions around parametrization in mind: should we invert for all the coefficients of the stiffness tensor or restrict to specific anisotropy type? Applications in the field of large-scale modelling for site effects in sedimentary basins to evaluate seismic hazard are also to be considered.

ACKNOWLEDGMENTS

This study was partially funded by the SEISCOPE consortium (http://seiscope2.osug.fr), sponsored by Aker BP, CGG, DUG, ExxonMobil, GEOLINKS, JGI, PETROBRAS, SHELL, SINOPEC and TOTALENERGIES. This study was granted access to the HPC resources provided by the GRICAD infrastructure (https://gricad.univ-grenoble-alpes.fr), which is supported by Grenoble research communities, the HPC resources of Cray Marketing Partner Network (https://partners.cray.com), and those of IDRIS/TGCC/CINES under the allocation 046091 made by GENCI. This work was partly funded by ANR (Agence Nationale pour la Recherche) ANR-16-CE31-0022-01 'HIWAI' project.

AUTHOR CONTRIBUTIONS

J. Cao (Conceptualization, Formal analysis, Investigation, Methodology, Software, Writing – original draft, Writing – review & editing), R. Brossier (Conceptualization, Formal analysis, Investigation, Methodology, Project administration, Software, Supervision, Writing – review & editing), Y. Capdeville (Conceptualization, Formal analysis, Investigation, Methodology, Project administration, Supervision, Writing – review & editing), L. Métivier (Conceptualization, Formal analysis, Investigation, Methodology, Project administration, Supervision, Writing – review & editing), S. Sambolian (Conceptualization, Formal analysis, Investigation, Methodology, Software, Writing – review & editing).

DATA AVAILABILITY

Data and code associated with this research belong to the SEISCOPE consortium. Any request related to the materials availability needs to be addressed to Romain Brossier (romain.brossier@univ-grenoblealpes.fr) or Ludovic Métivier (ludovic.metivier@univ-grenoblealpes.fr).

REFERENCES

Alder, C., Bodin, T., Ricard, Y., Capdeville, Y., Debayle, E. & Montagner, J., 2017. Quantifying seismic anisotropy induced by small-scale chemical heterogeneities, *Geophys. J. Int.,* **211**(3), 1585–1600.

Backus, G.E., 1962. Long-wave elastic anisotropy produced by horizontal layering, *J. geophys. Res.,* **67,** 4427–4440.

Bensoussan, A., Lions, J. & Papanicolaou, G., 1978. *Asymptotic Analysis of Periodic Structure,* North-Holland.

Bodin, T., Capdeville, Y., Romanowicz, B. & Montagner, J.-P., 2015. Interpreting radial anisotropy in global and regional tomographic models, in *The Earth's Heterogeneous Mantle: A Geophysical, Geodynamical, and Geochemical Perspective,* Springer Geophysics, pp. 105–144.

Bozdağ, E., Peter, D., Lefebvre, M., Komatitsch, D., Tromp, J., Hill, J., Podhorszki, N. & Pugmire, D., 2016. Global adjoint tomography: first-generation model, *Geophys. J. Int.,* **207**(3), 1739–1766.

Browaeys, J.T. & Chevrot, S., 2004. Decomposition of the elastic tensor and geophysical applications, *Geophys. J. Int.,* **159**(2), 667–678.

Burgos, G., Capdeville, Y. & Guillot, L., 2016. Homogenized moment tensor and the effect of near-field heterogeneities on nonisotropic radiation in nuclear explosion, *J. geophys. Res.: Solid Earth,* **121**(6), 4366–4389.

Cao, J., Brossier, R., Cabrera, E., de la Puente, J., Métivier, L. & Tarayoun, A., 2022a. GPU accelerated computing towards a fast and scalable seismic wave modelling in SEISCOPE SEM46 code, in *Sixth EAGE Workshop on High Performance Computing,* European Association of Geoscientists & Engineers.

Cao, J., Brossier, R., Górszczyk, A., Métivier, L. & Virieux, J., 2022b. 3D multi-parameter full-waveform inversion for ocean-bottom seismic data using an efficient fluid-solid coupled spectral-element solver, *Geophys. J. Int.,* **229**(1), 671–703.

Capdeville, Y., 2016. Non-periodic homogeneization for seismic forward and inverse problems, in *Methods and Challenges of Seismic Wave Modelling for Seismic Imaging Workshop, 78th Annual EAGE Meeting (Vienna)*.

Capdeville, Y., 2021. Homogenization of seismic point and extended sources, *Geophys. J. Int.,* **226**(2), 1390–1416.

Capdeville, Y. & Marigo, J.-J., 2007. Second order homogenization of the elastic wave equation for non-periodic layered media, *Geophys. J. Int.,* **170**(2), 823–838.

Capdeville, Y. & Marigo, J.-J., 2008. Shallow layer correction for spectral element like methods, *Geophys. J. Int.,* **172**(3), 1135–1150.

Capdeville, Y. & Marigo, J.-J., 2013. A non-periodic two scale asymptotic method to take account of rough topographies for 2-d elastic wave propagation, *Geophys. J. Int.,* **192**(1), 163–189.

Capdeville, Y. & Métivier, L., 2018. Elastic full waveform inversion based on the homogenization method: theoretical framework and 2-d numerical illustrations, *Geophys. J. Int.,* **213**(2), 1093–1112.

Capdeville, Y., Guillot, L. & Marigo, J.-J., 2010a. 1-D non-periodic homogenization for the seismic wave equation, *Geophys. J. Int.,* **181**(2), 897–910.

Capdeville, Y., Guillot, L. & Marigo, J.-J., 2010b. 2-D non-periodic homogenization to upscale elastic media for P-SV waves, *Geophys. J. Int.,* **182,** 903–922.

Capdeville, Y., Stutzmann, E., Wang, N. & Montagner, J.-P., 2013. Residual homogenization for seismic forward and inverse problems in layered media, *Geophys. J. Int.,* **194**(1), 470–487.

Capdeville, Y., Zhao, M. & Cupillard, P., 2015. Fast fourier homogenization for elastic wave propagation in complex media, *Wave Motion,* **54,** 170–186.

Capdeville, Y., Cupillard, P. & Singh, S., 2020. An introduction to the two-scale homogenization method for seismology, in *Advances in Geophysics,* Vol. **61,** Elsevier, pp. 217–306.

Chaljub, E., *et al.*, 2015. 3-D numerical simulations of earthquake ground motion in sedimentary basins: testing accuracy through stringent models, *Geophys. J. Int.,* **201**(1), 90–111.

Cupillard, P. & Capdeville, Y., 2018. Non-periodic homogenization of 3-D elastic media for the seismic wave equation, *Geophys. J. Int.,* **213**(2), 983–1001.

Cupillard, P., Mulder, W., Anquez, P., Mazuyer, A. & Barthélémy, J., 2020. The apparent anisotropy of the SEG-EAGE overthrust model, in *82th Annual EAGE Meeting (Amsterdam),* European Association of Geoscientists & Engineers.

Deville, M., Fischer, P. & Mund, E., 2002. *High Order Methods for Incompressible Fluid Flow,* Cambridge University Press, Cambridge.

Fichtner, A. & Villaseñor, A., 2015. Crust and upper mantle of the western mediterranean – constraints from full-waveform inversion, *Earth planet. Sci. Lett.,* **428,** 52–62.

Fichtner, A., Kennett, B.L. & Trampert, J., 2013. Separating intrinsic and apparent anisotropy, *Phys. Earth planet. Inter.,* **219,** 11–20.

Hestenes, M.R. & Stiefel, E., 1952. Methods of conjugate gradient for solving linear systems, *J. Res. Nat. Bur. Stand.,* **49,** 409–436.

Ide, S., Baltay, A. & Beroza, G.C., 2011. Shallow dynamic overshoot and energetic deep rupture in the 2011 mw 9.0 tohoku-oki earthquake, *Science,* **332**(6036), 1426–1429.

Karaoğlu, H. & Romanowicz, B., 2018. Inferring global upper-mantle shear attenuation structure by waveform tomography using the spectral element method, *Geophys. J. Int.,* **213**(3), 1536–1558.

Kennedy, J. & Eberhart, R., 1995. Particle swarm optimization, in *Proceedings of ICNN'95 - International Conference on Neural Networks,* Vol. **4,** pp. 1942–1948.

Komatitsch, D., 1997. *Méthodes spectrales et éléments spectraux pour l'équation de l'élastodynamique 2D et 3D en milieu hétérogène,* PhD thesis, Institut de Géophysique du Globe de Paris.

Komatitsch, D. & Vilotte, J.P., 1998. The spectral element method: an efficient tool to simulate the seismic response of 2D and 3D geological structures, *Bull. seism. Soc. Am.,* **88,** 368–392.

Lei, W., *et al.*, 2020. Global adjoint tomography—model glad-m25, *Geophys. J. Int.,* **223**(1), 1–21.

Li, Y., Brossier, R. & Métivier, L., 2020. 3D frequency-domain elastic wave modeling with spectral-element method using a massively parallel direct solver, *Geophysics,* **85**(2), T71–T88.

Lu, Y., Stehly, L., Brossier, R., Paul, A. & Group, A.W., 2020. Imaging Alpine crust using ambient noise wave-equation tomography, *Geophys. J. Int.,* **222**(1), 69–85.

Magali, J., Bodin, T., Hedjazian, N., Ricard, Y., Capdeville, Y. & Debayle, E., 2021. Quantifying intrinsic and extrinsic contributions to radial anisotropy in tomographic models, *J. geophys. Res.: Solid Earth,* **126**(10), e2021JB022322, doi: 10.1029/2021JB022322.

Martin, G.S., Wiley, R. & Marfurt, K.J., 2006. Marmousi2: an elastic upgrade for Marmousi, *Leading Edge,* **25**(2), 156–166.

Moulinec, H. & Suquet, P., 1998. A numerical method for computing the overall response of nonlinear composites with complex microstructure, *Comput. Method. Appl. Mech. Eng.,* **157**(1-2), 69–94.

Oristaglio, M., 2012. SEAM phase II—land seismic challenges, *Leading Edge,* **31**(3), 264–266.

Patera, A.T., 1984. A spectral element method for fluid dynamics: laminar flow in a channel expansion, *J. Comput. Phys.,* **54,** 468–488.

Sánchez-Palencia, E., 1980. Non-homogeneous media and vibration theory, in *Lecture Note in Physics,* Vol. **320**. Springer-Verlag, pp. 57–65.

Schenk, O. & Gärtner, K., 2011. *PARDISO,* Springer US, Boston, MA. pp. 1458–1464.

Tang, J.H., Brossier, R. & Métivier, L., 2022. Fully scalable solver for frequency-domain visco-elastic wave equations in 3D heterogeneous media: a controllability approach, *J. Comput. Phys.,* **468,** 111514, doi: 10.1016/j.jcp.2022.111514.

Tarayoun, A., Brossier, R., Cao, J., Jauré, S., Laforêt, S. & Métivier, L., 2022. HPC implementations on SEM46: a 3D modeling and inversion code for anisotropic visco-elastic coupled acoustic media, in *Sixth EAGE Workshop on High Performance Computing,* European Association of Geoscientists & Engineers.

Thrastarson, S., van Herwaarden, D.-P., Krischer, L., Boehm, C., van Driel, M., Afanasiev, M. & Fichtner, A., 2022. Data-adaptive global full-waveform inversion, *Geophys. J. Int.,* **230**(2), 1374–1393.

Trinh, P.T., Brossier, R., Métivier, L., Virieux, J. & Wellington, P., 2017. Bessel smoothing filter for spectral element mesh, *Geophys. J. Int.,* **209**(3), 1489–1512.

Trinh, P.T., Brossier, R., Métivier, L., Tavard, L. & Virieux, J., 2019. Efficient 3D time-domain elastic and viscoelastic Full Waveform Inversion using a spectral-element method on flexible Cartesian-based mesh, *Geophysics,* **84**(1), R75–R97.

Virieux, J., Asnaashari, A., Brossier, R., Métivier, L., Ribodetti, A. & Zhou, W., 2017. An introduction to full waveform inversion, in *Encyclopedia of Exploration Geophysics,* pp. R1–1-R1-40, eds Grechka, V. & Wapenaar, K., Society of Exploration Geophysics.

Wang, N., Montagner, J.-P., Fichtner, A. & Capdeville, Y., 2013. Intrinsic versus extrinsic seismic anisotropy: the radial anisotropy in reference earth models, *Geophys. Res. Lett.,* **40**(16), 4284–4288.

Wells, W.M., 1986. Efficient synthesis of Gaussian filters by cascaded uniform filters, *IEEE Trans. Pattern Anal. Mach. Intell.,* **PAMI-8**(2), 234–239.

Yuan, H., French, S., Cupillard, P. & Romanowicz, B., 2014. Lithospheric expression of geological units in central and eastern North America from full waveform tomography, Special issue on USArray science, *Earth planet. Sci. Lett.,* **402,** 176–186.